Budapest University of Technology and Economics
Faculty of Electrical Engineering and Informatics
Department of Telecommunications

Péter Rucz

Determination of acoustic parameters of organ pipes by means of numerical techniques

Master's Thesis

Supervisors

Assoc. Prof. Fülöp Augusztinovicz
Dr. Péter Fiala
Dr. Judit Angster (Fraunhofer Institut für Bauphysik)

BUDAPEST, 2009

Nyilatkozat

Alulírott **Rucz Péter**, a Budapesti Műszaki és Gazdaságtudományi Egyetem Villamosmérnöki és Informatikai Kar hallgatója kijelentem, hogy ezt a diplomatervet meg nem engedett segítség nélkül, saját magam készítettem, és a diplomatervben csak a megadott forrásokat használtam fel. Minden olyan részt, melyet szó szerint, vagy azonos értelemben, de átfogalmazva más forrásból átvettem, egyértelműen, a forrás megadásával megjelöltem.

Kelt: Budapest, 2009. 05. 13.

. . . . . .

Rucz Péter

Kivonat

Az orgonasípok hangkeltési mechanizmusa rendkívül bonyolult fizikai folyamat, mivel akusztikai és áramlástani jelenségek párhuzamosan, csatolva jelennek meg. Ennek ellenére, pusztán akusztikai rezonátorként modellezve a sípot, megfelelő pontossággal becsülhetjük a hangzás több kulcsfontosságú paraméterét. Jelen mű célja az orgonasípok szimulációjára alkalmas numerikus technikák bemutatása. Munkám során többféle numerikus eljárást használtam a modellezéshez, melyeket kereskedelmi és saját fejlesztésű szoftverekkel valósítottam meg. A szimulációk eredményeit analitikus számításokkal és mérési adatokkal vetettem össze. Megmutattam, hogy a numerikus technikák jól alkalmazhatóak a síp főbb akusztikai paramétereinek meghatározására.

Abstract

The sound generation of an organ pipe is a very complex physical process, since the acoustical phenomena take place coupled with fluid flow effects. Even so, by modeling the organ pipe merely as an acoustic resonator, one can predict several key parameters of the sounding with sufficient accuracy. The aim of this work is to examine the simulation techniques that can be used for organ pipe modeling. In the course of the work reported herein, I have modeled organ pipes by means of various numerical techniques. Commercial and self-developed software packages were used, and the obtained data were compared with analytical solutions and measurement results. It was shown that by using these techniques one can approximate key acoustic parameters of the pipe.

Contents

List of Figures

List of Tables

Chapter 1

Introduction

1.1 Motivation

Scaling of organ pipes is still performed according to the rules laid down in the 19th century. These rules prescribe pipe dimensions for the desired sounding, but in some cases changing the traditional geometry parameters is inevitable (for aesthetic and practical reasons). Then the organ builder can only rely on his experience, attempting to tune the sounding parameters of the pipe.

The aim of applying numerical techniques for organ pipe simulation is twofold. On the one hand to speed up the scaling and tuning process, saving quite some time for organ manufacturers as an organ consists of thousands of pipes. On the other hand it will hopefully help developing new scaling methods. The purpose of the latter is to predict, how the traditional organ sounds can be preserved with changed geometrical parameters, and how new sounding characteristics can be achieved.

Since the computational capacity of computers has augmented exponentially in the last few decades, more and more accurate models can be examined by computer simulations. While analytical computations are limited to the simplest cases, problems that can be solved by numerical techniques can be much more complicated. The other reason why simulations get a wider and wider scope, is that they are more cost and time effective than prototyping for example.

As the sound generation mechanism of a pipe organ is a very complex physical process, one should apply significant simplifications to be able to model the problem by means of numerical techniques of linear acoustics. Despite of the fact, that these simplifications could be very rough in certain cases, some key information on the sounding can be determined by using simplified numerical models in simulations. When comparing the results with measurement data, the effects of the applied simplifications and neglects should always be taken into consideration.

As a validation of the model, the results should be compared to measurement data whenever it is possible.

In the course of the work the author has implemented organ pipe simulations by various numerical techniques using commercial and self developed software. Simulation results were compared with analytical solutions and measurements. This work was performed at the Budapest University of Technology and Economics, Department of Telecommunications, Laboratory of Acoustics.

1.2 Aim of the thesis

This thesis was aimed to show that numerical techniques can be applied for acoustical modeling of organ pipes, and by using these methods some key parameters of the sounding can be determined with sufficient accuracy.

The objectives of this project were the following:

- Analysis of the sound generation mechanism of pipe organs and the characteristics of the steady sound field spectra.
- Detailed examination of numerical methods in linear acoustics. Understanding the FEM and BEM techniques, deducing the solution for a coupled FE/BE method. Exploration of the scientific literature concerning novel techniques, such as ABC and PML.
- Setting up pipe meshes with different geometry parameters for various pipe types. Simulation of organ pipes by using commercial software packages as well as self developed software.
- Comparison of the results of simulations implemented by different methods with each other and measurement data, and examination the accuracy of the simulations.
- Experimenting the PML for a simple case with different parameters.

1.3 Thesis outline

The work process of this thesis is shown in figure 1.1. As seen, achievements are based on a remarkable scientific basis and a priori knowledge. The arrows in the figure represent these connections. Since developments rely on the scientific basis in substances – and intermediary outcomes are also made use of – basics of linear acoustics and two fundamental numerical methods are also examined here. Accordingly, this thesis is structured as follows

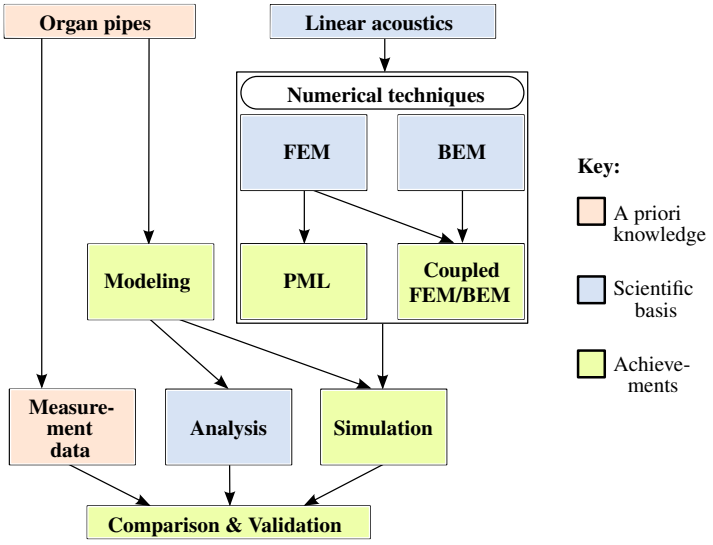

Figure 1.1: Work process of this thesis

Chapter 2 summarizes functional principles of pipe organs. The structure of the pipe organ, pipe configurations and attributes of the steady sound characteristics are examined.

Chapter 3 gives an approach to the numerical techniques in acoustics. From the fundamental relations and basics of linear acoustics the weak form of the boundary value problem is derived, which is the first base of the discretization.

Chapter 4 explains numerical techniques in linear acoustics. The finite and the boundary element method is discussed in detail, and a coupled technique is derived based on these two methods. Finally, perfectly matched layers are introduced, as an alternative way of modeling exterior problems.

Chapter 5 focuses on the modeling of the organ pipe simulation problem. Therein, simulation setup and the applied and developed software is explained.

Chapter 6 presents the simulation results. Starting from the first steps, impedance analysis and pipe simulations are discussed in detail. PML experiments are also described here.

Chapter 7 gives conclusion and outlook on further work.

Chapter 2

Organs and organ sound

2.1 Preliminaries

There are a great variety of musical instruments that are referred to by the term 'organ', such as pipe organs, positive organs, chord organs, Hammond and digital organs among others. However, the most well-known and original type of organ is the pipe organ, which is usually played in many church services and classical music concerts. This thesis also deals with organs of this type.

The pipe organ is a keyboard instrument played using one or more manuals and a pedal board. It is classified into the aerophones group, as it produces sound by vibrating columns of air. The wind moving through metal or wooden pipes remains constant while a key is depressed.

Organ building is a traditional industrial sector in Europe. The competitiveness of the organ builder is principally determined by the quality of his pipe organs. About them, two quality aspects can be named. On the one hand, the organ has to be understood as a sophisticated and complex engineering work. Therefore, its excellence lies in its technical quality. On the other hand, as a musical instrument the pipe organ has to show its aesthetic quality through its sound quality. In fact, the sound quality is the essence of the organ builder, the personal signature which earns his reputation.

The sound quality of the pipe ranks depends on the dimensioning (or scaling) of the pipes and on the voicing adjustment. Scaling concerns all about selecting geometrical parameters of the pipe, whereas voicing refers to tuning, the process of adjusting the parts of the pipe to produce the desired tone. The aim of scaling and voicing is to ensure the required quality of the perceived sound.

The quality of the produced sound can be characterized by various acoustical parameters that typify many aspects of the sounding. In the following only the

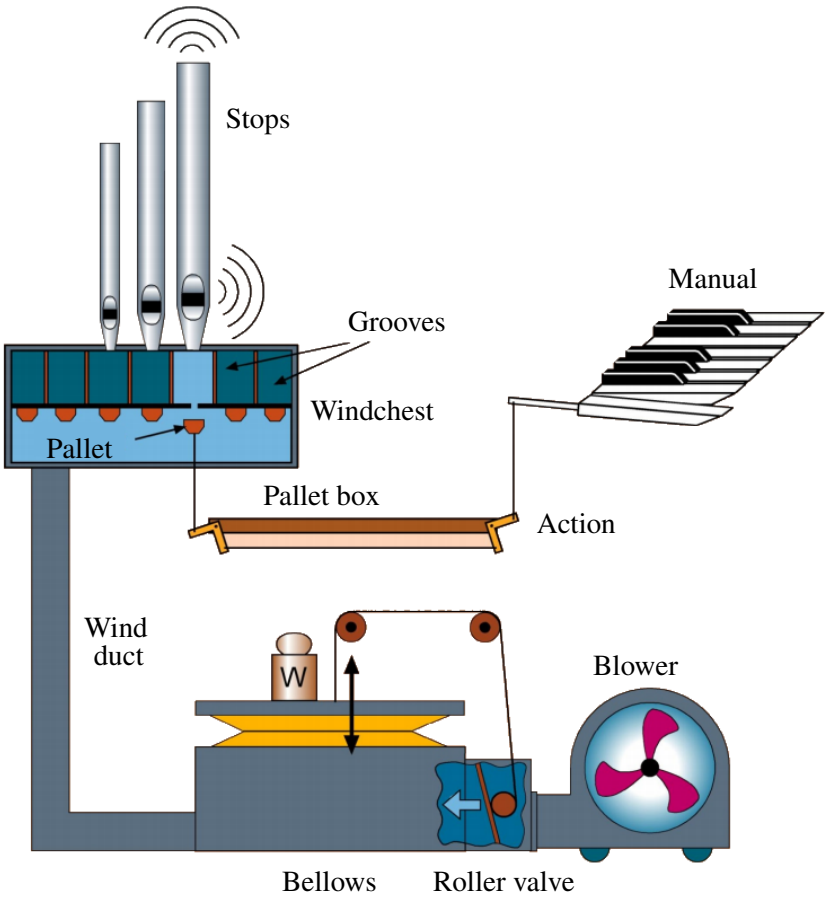

Figure 2.1: Mechanical structure of an organ pipe. (Source: [14])

most important ones will be introduced, which give key information on the steady sound spectrum. To understand these factors of the sound quality, the functional principles and the fundamentals of the sound generation mechanism should be examined.

2.2 Structure and sound generation mechanism

The essential parts of a pipe organ can be seen in fugure 2.1. The sound is produced when the wind passes through the pipes. The process of transferring the wind to a pipe begins when the blower inserts air into the bellows.

The air flows from the bellows into the windchest through several wind ducts. The windchest is a plain wooden box with rows of holes on the top. The pipes stand on its top, one pipe to each hole. To make the pipe sound, the wind must still move from the windchest to the pipe. It happens as follows: when a key is pressed, the action (or tracker) pulls the pallet down, the groove opens and allows the wind to enter the pipe. When the pipe is not being played the pallet closes the hole of the corresponding pipe.

There are endless types of configuration and structure for organ pipes, whose main distinguishing features are: material (wood or metal), form of the resonator (cylindrical, conical or rectangular), sort of excitation (reed pipe or flue pipe) and ending of the resonator (open or closed – also known as gedackt or stopped). Longitudinal sections of a cylindrical metal and a rectangular wooden flue pipe can be seen in figure 2.2.

Two main parts of the pipes are the foot and the body or resonator. The foot constitutes the bottom part of the pipe. At the foot base is the foot hole or the bore, through which wind gets into the pipe. The length of the pipe foot does not modify the pitch. Therefore, organ builders design the foot lengths of their pipes depending on several factors. The length and volume of the resonator and the voicing determine the fundamental pitch and timbre of the pipe.

The mouth of the pipe is the horizontal opening cut at the joint between the body and the foot and is delimited by the upper and the lower lips. At this joint a sheet of metal or wood called languid is attached horizontally inside the pipe. The languid divides the resonator and the foot completely, except for a small groove parallel to the mouth named windway. This separation creates a cavity inside the pipe foot, which allows air to flow into the resonator from the foot, but only as a thin jet of wind directed towards the mouth.

The air jet that evolves in the windway starts to oscillate around the upper lip, and this vibrating movement of air provides the excitation of the air column resonating inside the pipe body. This air column can resonate at different characteristic resonant frequencies.

As seen, the sound generation process of an organ pipe is a very complex physical procedure as the acoustic phenomena show up coupled with fluid flow effects. The examination of this problem in full detail would require the analysis of a coupled non-linear acoustic and fluid flow model. At the same time, some key parameters of the sounding can be obtained if the pipe is regarded merely as an acoustic resonator. By this simplification, transient attacks can not be taken into consideration, our experiments are limited to the examination of stationary spectra. The stationary sound spectra of an organ pipe is mostly determined by the transfer function of the pipe resonator.

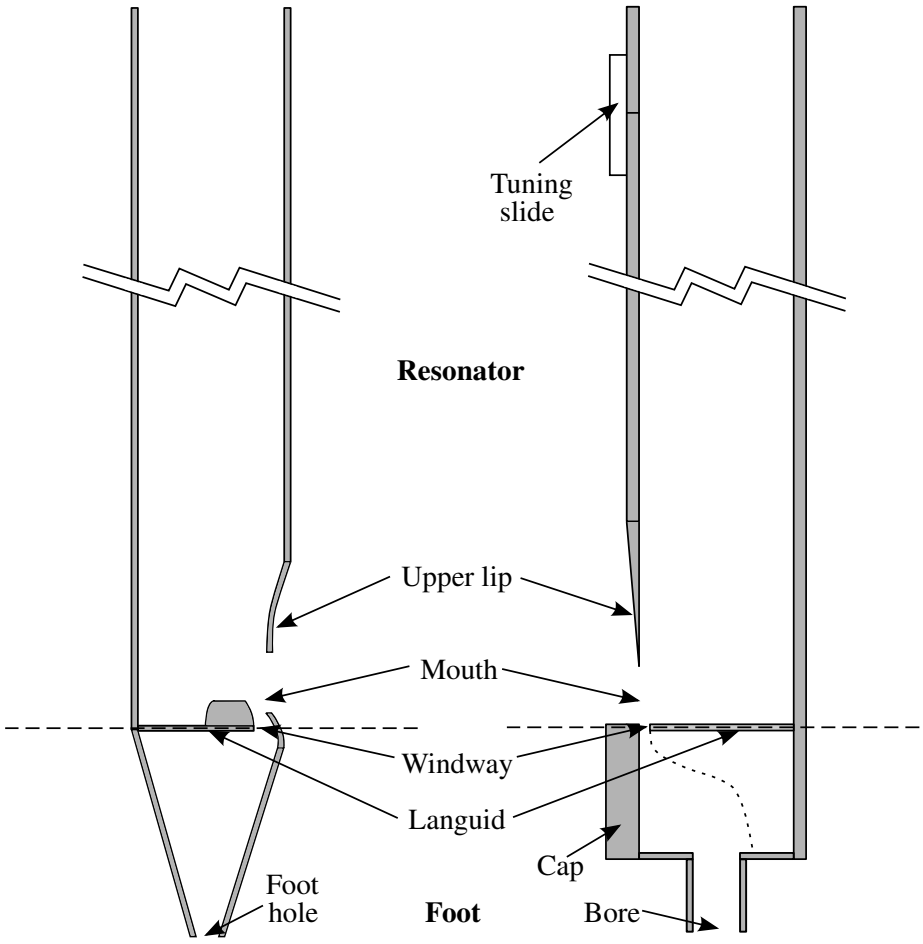

Figure 2.2: Longitudinal section of a cylindrical metal (left) and a rectangular wooden (right) flue organ pipe

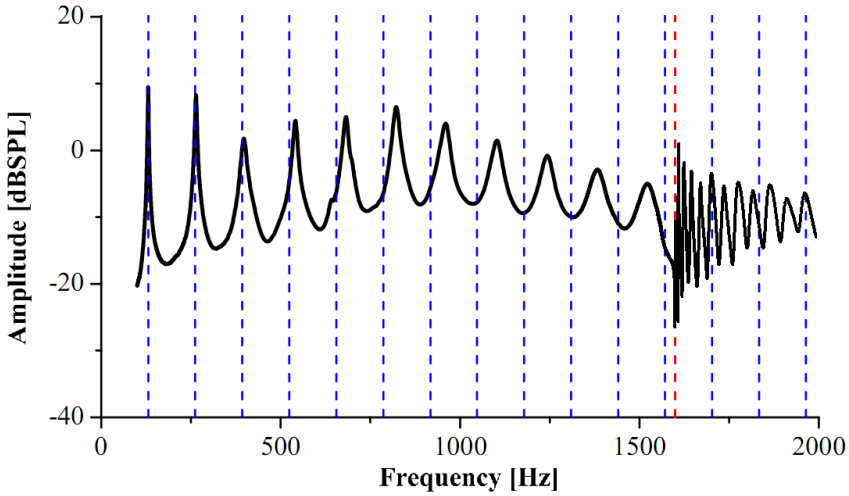

Figure 2.3: Typical transfer function of an organ pipe. Blue dashed lines show the exact harmonics of the first resonant frequency. Red dashed line denotes the cut-off frequency.

2.3 Characteristics of the pipe transfer function

The transfer function of the pipe determines that how the resonator will react to the excitation respect to the frequency. The geometry of the resonator determines the frequencies of eigenresonances, i.e. the frequencies at which the air column inside the body can resonate at. At these eigenfrequencies the transfer function shows peaks of significant amplification. A typical organ pipe transfer function can be seen in figure 2.3.

The transfer function of the resonator also determines the characteristics of the steady sound spectrum. Therefore, key information on the sounding can be obtained by the analysis of the pipe transfer function. This data can be summarized by the following acoustical parameters.

- **Fundamental frequency**

  This is the first resonant frequency of the pipe. Even though, other harmonics can be more dominant during transient attacks (see [14, 29]), it is the fundamental frequency that determines the tone of the pipe. This frequency has the highest amplitude in the stationary sound spectra.

- **Frequencies of harmonic partials**

  As can be seen in figure 2.3, in case of an organ pipe, the eigenresonances are not exact harmonics of the first resonance. The frequencies of these modes

are slightly stretched. This effect is called stretching and it is an important attribute of the organ sound. The stretching effect is especially sensitive to the geometry parameters of the pipe (see [29]). Generally, stretching values are higher of pipes with larger diameter.

- **Q-factors of eigenresonances**

  The peaks of harmonic partials are not equally sharp. Q-factors are higher in case of the first few harmonics and lower for the further harmonics. This means that amplification peaks become wider for the successive harmonics. Q-factors are also dependent of the resonator geometry. Larger diameter results in lower Q-factor in general.

- **Cut-off frequency**

  Since the diameter (or depth, e.g. in case of wooden pipes) of an organ pipe is much smaller than its length, pure longitudinal eigenmodes appear at lower frequencies. The frequency, where transversal resonances start to appear, is called cut-off frequency as the sound spectrum above this frequency shows irregularities compared to the slightly stretched harmonic peaks at lower frequencies. These irregularities are caused by the combined excitation of longitudinal and transversal modes.

The explanation of these characteristics will be discussed in chapter 6. There are many other attributes of the organ sound, which are not examined here. A more detailed review on the sound generation process and organ sound including the examination of attack transients can be found in [1], [14] or [29].

Chapter 3

An approach to numerical techniques in acoustics

This chapter summarizes the physical and mathematical concepts of linear acoustics. From the fundamental laws of continuum mechanics the wave equation will be derived. Introducing boundary conditions the weak form of the Helmholtz equation will be deduced, which is the first step of the discretization process of numerical techniques discussed in the forthcoming chapters.

3.1 Governing equations of the sound field

The approach to the wave equation will be discussed as in [23]. The deduction will be described in detail as some of the results will be needed in further chapters.

Fundamentals of linear acoustics are based on the basic equations of continuum mechanics. It is assumed that the dimensions of the problem are large compared to the size of molecules. For the derivation of the wave equation the Eulerian representation and spatial coordinates will be used.

We consider problems defined over domain Ω. The complement of this domain is denoted as Ω_c. Boundary of these two domains is represented by Γ. This configuration includes the direction of the outward normal, pointing into Ω_c as shown in figure 3.1. These and the further notations are accepted and used in the scientific literature of acoustics.

3.1.1 Fundamental axioms of continuum mechanics

The wave equation can be derived from two fundamental laws of the theory of continuum mechanics. These two are the principle of conversation of mass and the

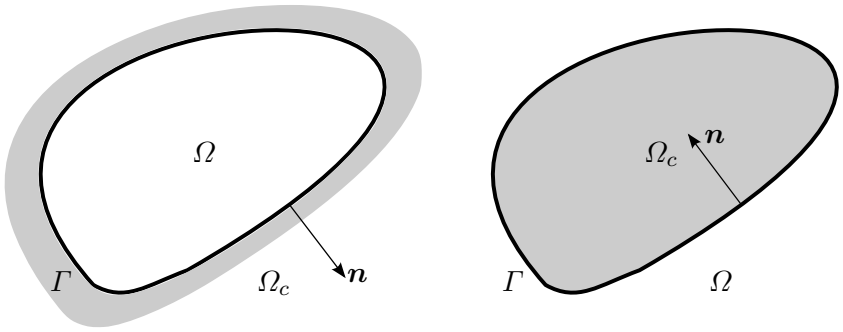

(a) interior problem (b) exterior problem

Figure 3.1: Definitions of regions Ω and Ω_c, boundary Γ and outward normal vector $\boldsymbol{n}$.

principle of balance of momentum.

Conservation of mass

The principle of conversation of mass means that the total mass M in the considered domain Ω

$$M(t) = \int_{\Omega} \varrho(\boldsymbol{x}, t) \mathrm{d}\boldsymbol{x} \tag{3.1}$$

remains constant during the motion, where $\boldsymbol{x}$ and t denote position vector and time. Often, these dependencies will not be shown in the equations. The principle of conversation of mass implies that the material derivative (or total time derivative) vanishes, i.e.

$$\dot{M} = \frac{\mathrm{d}M}{\mathrm{d}t} = \int_{\Omega} \left(\frac{\partial \varrho}{\partial t} + \boldsymbol{\nabla} \varrho \cdot \boldsymbol{v} \right) \mathrm{d}\boldsymbol{x} = 0. \tag{3.2}$$

The material derivative introduces the flow velocity vector $\boldsymbol{v}$ which results from $\partial \boldsymbol{x} / \partial t$. In addition of the global validity of the conservation of mass, we require that it is also valid for an arbitrarily small neighborhood of each material point, which implies the local conversation of mass as

$$\frac{\partial \varrho}{\partial t} + \boldsymbol{\nabla} \varrho \cdot \boldsymbol{v} = 0. \tag{3.3}$$

Balance of momentum

The principle of balance of momentum means that the time rate of change of momentum is equal to the resultant force $\boldsymbol{F}_R$ acting on the body. With momentum

vector $\boldsymbol{P}$, also known as the linear momentum vector, this is written as

$$\dot{\boldsymbol{P}} = \frac{\mathrm{d}\boldsymbol{P}}{\mathrm{d}t} = \boldsymbol{F}_R. \tag{3.4}$$

Herein, the momentum vector is given by

$$\boldsymbol{P} = \int_\Omega \varrho \boldsymbol{v} \mathrm{d}\boldsymbol{x} \tag{3.5}$$

whereas the resultant force combines volume forces and external forces as

$$\boldsymbol{F}_R = \int_\Omega \boldsymbol{b}\varrho \mathrm{d}\boldsymbol{x} - \int_\Gamma p\boldsymbol{n} \mathrm{d}\boldsymbol{x}. \tag{3.6}$$

In equation (3.6), the first term on the right hand side is known as the resultant external body force with the external body force $\boldsymbol{b}$. Using this term, we may consider gravity effects, for example. In linear acoustics this term is usually not relevant and, consequently, zero. The second term represents the resultant contact force which can be transformed into a domain integral by application of Gauss' theorem:

$$\int_\Gamma p\boldsymbol{n} \mathrm{d}\boldsymbol{x} = \int_\Omega \boldsymbol{\nabla} p \mathrm{d}\boldsymbol{x}. \tag{3.7}$$

The material derivative of momentum is given as

$$\begin{aligned} \frac{\mathrm{d}\boldsymbol{P}}{\mathrm{d}t} = \frac{\mathrm{d}}{\mathrm{d}t}\left(\int_\Omega \varrho \boldsymbol{v} \mathrm{d}\boldsymbol{x}\right) = \int_\Omega \frac{\mathrm{d}(\varrho \boldsymbol{v})}{\mathrm{d}t} \mathrm{d}\boldsymbol{x} = \\ = \int_\Omega \left[\frac{\partial \varrho}{\partial t}\boldsymbol{v} + \varrho \frac{\partial \boldsymbol{v}}{\partial t} + (\boldsymbol{\nabla}\varrho \cdot \boldsymbol{v} + \boldsymbol{\nabla} \cdot \boldsymbol{v}\varrho)\boldsymbol{v}\right] \mathrm{d}\boldsymbol{x}. \end{aligned} \tag{3.8}$$

The first and the third terms of the integrand vanish with respect to the conversation of mass in equation (3.2) and (3.3), respectively. This yields

$$\frac{\mathrm{d}\boldsymbol{P}}{\mathrm{d}t} = \int_\Omega \left[\varrho \frac{\partial \boldsymbol{v}}{\partial t} + \boldsymbol{\nabla} \cdot \boldsymbol{v}\varrho\boldsymbol{v}\right] \mathrm{d}\boldsymbol{x}. \tag{3.9}$$

Summarizing these manipulations, we incorporate equation (3.6), (3.7) and (3.9) into equation (3.4) to obtain the so-called Euler equation

$$\int_\Omega \left[\varrho \frac{\partial \boldsymbol{v}}{\partial t} + \boldsymbol{\nabla} \cdot \boldsymbol{v}\varrho\boldsymbol{v} + \boldsymbol{\nabla} p\right] \mathrm{d}\boldsymbol{x} = 0 \tag{3.10}$$

or, in local form,

$$\varrho \frac{\partial \boldsymbol{v}}{\partial t} + \boldsymbol{\nabla} \cdot \boldsymbol{v}\varrho\boldsymbol{v} + \boldsymbol{\nabla} p = 0. \tag{3.11}$$

In continuum mechanics, Euler's equations of motion comprise the balance of momentum and the balance of momentum of momentum, also known as the balance of angular momentum. The latter axiom can be neglected since shear effects are not considered herein. Euler's equation (3.11) can be considered as a special local form of Newton's equation of motion $\boldsymbol{F}_R = \partial(m\boldsymbol{v})/\partial t$.

Linearization and simplification

Commonly, problems of linear acoustics refer to small perturbations of ambient quantities. These ambient quantities are referred to by using the subscript 0. The small fluctuating parts of pressure, density and flow velocity vector are represented as $\tilde{p}$, $\tilde{\varrho}$ and $\tilde{\boldsymbol{v}}$. With this notation, we can substitute for the quantities pressure, density and flow velocity as

$$\begin{aligned} p &= p_0 + \tilde{p}, \\ \varrho &= \varrho_0 + \tilde{\varrho}, \\ \boldsymbol{v} &= \boldsymbol{v}_0 + \tilde{\boldsymbol{v}}. \end{aligned} \tag{3.12}$$

For simplicity for the wave equation approach, we assume that there is no ambient flow, i.e. $\boldsymbol{v}_0 = \boldsymbol{0}$.

Substituting for the major quantities in equation (3.3) and considering only first order terms, we write

$$\frac{\partial \tilde{\varrho}}{\partial t} + \varrho_0 \boldsymbol{\nabla} \cdot \tilde{\boldsymbol{v}} = 0. \tag{3.13}$$

Similarly, Euler's equation (3.11) is linearized and simplified as

$$\varrho_0 \frac{\partial \tilde{\boldsymbol{v}}}{\partial t} + \boldsymbol{\nabla} \tilde{p} = 0, \tag{3.14}$$

where it is assumed that ϱ_0 and p_0 are independent of time and spatial coordinates.

3.1.2 Consecutive equation

In fluids, sound propagates through pressure waves only. The velocity of the sound pressure wave – better known as the speed of sound – depends on the propagation material. For wave propagation in linear fluid acoustics, the speed of sound is one of the relevant material parameters. It can be understood as the result of mathematical relations of other material parameters which are not solely relevant for our considerations.

The consecutive relations are usually referred to as the equations of state. With respect to thermodynamics, the pressure fluctuation and, thus, sound propagation occurs with negligible heat flow because the changes of the state occur so rapidly

that there is no time for the temperature to equalize with the surrounding medium. This is the property of an adiabatic process. If fluctuation amplitudes and frequency remain small enough, the process can be considered as reversible and isotropic.

Derivation of the speed of sound is different for gases, liquids and solids. Since we limit our considerations to air herein, we will only discuss derivation of the speed of sound for gases in what follows.

The speed of sound c may be introduced as a constant to relate the fluctuating parts of pressure and density to each other as

$$\tilde{p} = c^2 \tilde{\varrho}. \tag{3.15}$$

This is equivalent to

$$c = \sqrt{\frac{\partial p}{\partial \varrho}}. \tag{3.16}$$

Gases

We consider ideal gases only. With the specific heat ration κ, an adiabatic process implies the relation $p\varrho^{-\kappa} = \text{constant}$. Since this relation is valid at any time, it implies first

$$(p_0 + \tilde{p})(\varrho_0 + \tilde{\varrho})^{-\kappa} = p_0 \varrho^{-\kappa} \tag{3.17}$$

and is rewritten as

$$1 + \frac{\tilde{p}}{p_0} = \left(1 + \frac{\tilde{\varrho}}{\varrho_0}\right)^{\kappa}. \tag{3.18}$$

The right hand-side is linearized by

$$\left(1 + \frac{\tilde{\varrho}}{\varrho_0}\right)^{\kappa} \approx 1 + \kappa \frac{\tilde{\varrho}}{\varrho_0}, \tag{3.19}$$

which simplifies equation (3.18) yielding

$$\tilde{p} = \left(\kappa \frac{p_0}{\varrho_0}\right) \tilde{\varrho} = c^2 \tilde{\varrho}, \tag{3.20}$$

where the speed of sound is denoted by c. The variable K denoting the adiabatic bulk modulus is introduced as

$$c = \sqrt{\frac{K}{\varrho_0}} = \sqrt{\frac{\kappa p_0}{\varrho_0}}. \tag{3.21}$$

Similar relation can be derived for liquids, but we consider gases only.

3.1.3 Derivation of the wave equation

It is useful for further description to reduce the problem to one variable. Herein, this variable will be the pressure fluctuation which will be referred to as the sound pressure in what follows. The local conversation of mass (3.3) in its linearized form (3.13), the Euler equation as the balance of momentum (3.11) in its linearized form (3.14) and the consecutive relation of equation (3.15) are all summarized into one partial differential equation, i.e. the wave equation.

For that, we start at the consecutive relation (3.15) which is differentiated twice respect to time

$$\frac{\partial^2 \tilde{p}}{\partial t^2} = c^2 \frac{\partial^2 \tilde{\varrho}}{\partial t^2}. \tag{3.22}$$

Then, derivatives of the density fluctuations are replaced by the local conversation of mass in linearized form (3.13) which gives

$$\frac{\partial^2 \tilde{p}}{\partial t^2} = -c^2 \varrho_0 \frac{\partial(\boldsymbol{\nabla} \cdot \tilde{\boldsymbol{v}})}{\partial t} = -c^2 \varrho_0 \boldsymbol{\nabla} \cdot \left(\frac{\partial \tilde{\boldsymbol{v}}}{\partial t} \right). \tag{3.23}$$

Finally, the linearized Euler equation (3.14) is used to substitute the velocity vector as

$$\frac{\partial^2 \tilde{p}}{\partial t^2} = c^2 \boldsymbol{\nabla} \cdot \boldsymbol{\nabla} \tilde{p}. \tag{3.24}$$

Equation (3.24) is known as the wave equation. Mostly the scalar product $\boldsymbol{\nabla} \cdot \boldsymbol{\nabla}$ is replaced by the Laplacian Δ. The wave equation is a hyperbolic partial differential equation.

3.1.4 Equations in the frequency domain

In the following, the governing equations of the sound field will be transformed into the frequency domain by means of Fourier transform. The Fourier transform of the sound pressure is defined as

$$p(\boldsymbol{x}, t) = \frac{1}{2\pi} \int_{-\infty}^{\infty} \hat{p}(\boldsymbol{x}, \omega) \mathrm{e}^{\mathrm{i}\omega t} \mathrm{d}\omega \tag{3.25}$$

and

$$\hat{p}(\boldsymbol{x}, \omega) = \int_{-\infty}^{\infty} p(\boldsymbol{x}, t) \mathrm{e}^{-\mathrm{i}\omega t} \mathrm{d}t. \tag{3.26}$$

The hat on a value notates complex amplitude in the frequency domain. For simplicity in further analysis we will use the notation: $\hat{p}(\boldsymbol{x}, \omega) = \hat{p}(\boldsymbol{x}) = \hat{p}$ and similarly $\hat{\boldsymbol{v}}(\boldsymbol{x}, \omega) = \hat{\boldsymbol{v}}(\boldsymbol{x}) = \hat{\boldsymbol{v}}$.

By substituting the transformed variables into the governing equations of the sound field, equations (3.13) and (3.14) can be rewritten in the frequency domain. The linearized form of conversation of mass can be described as

$$\mathrm{i}\omega\hat{\varrho} + \varrho_0 \boldsymbol{\nabla} \cdot \hat{\boldsymbol{v}} = 0, \tag{3.27}$$

and similarly the Euler equation reads as

$$\mathrm{i}\omega\varrho_0\hat{\boldsymbol{v}} + \boldsymbol{\nabla}\hat{p} = 0. \tag{3.28}$$

From these two equations the Helmholtz equation, or reduced wave equation can directly be derived by making use of equation (3.15). The Helmholtz equation is given as

$$\Delta\hat{p}(\boldsymbol{x}) + k^2\hat{p}(\boldsymbol{x}) = 0. \tag{3.29}$$

Here, the wave-number $k = \omega/c$ is the quotient of the circular frequency $\omega = 2\pi f$ (f denoting frequency) and the speed of sound c.

3.2 The boundary value problem

3.2.1 Partial differential equation and boundary condition

The wave equation (3.24)

$$\Delta\tilde{p}(\boldsymbol{x}, t) = \frac{1}{c^2}\frac{\partial^2\tilde{p}(\boldsymbol{x}, t)}{\partial t^2} \qquad \boldsymbol{x} \in \Omega \subset \mathbb{R}^d \tag{3.30}$$

is valid for the sound pressure $\tilde{p}$. Alternatively, a velocity potential may be used. The space dimension d is three in real applications, but can be two or one in certain cases. To complete a solution, the differential equation requires boundary conditions and initial conditions, which will be specified when used.

Boundary conditions will be introduced as follows. The region of interest, Ω has a common boundary, $\Gamma_s \subseteq \Gamma$ with a mechanical structure. Boundary conditions prescribe the relation between normal velocities of the mechanical structure and fluid (v_s and v_f) for every point of Γ_s. Herein, v_s is known, while v_f is unknown. This setup is shown in figure 3.2.

We assume admittance boundary conditions being equivalent to Robin boundary conditions, which may degenerate to Neumann boundary conditions if the admittance is zero.

$$v_f(\boldsymbol{x}) - v_s(\boldsymbol{x}) = Y(\boldsymbol{x})p(\boldsymbol{x}) \qquad \boldsymbol{x} \in \Gamma \subset \mathbb{R}^d \tag{3.31}$$

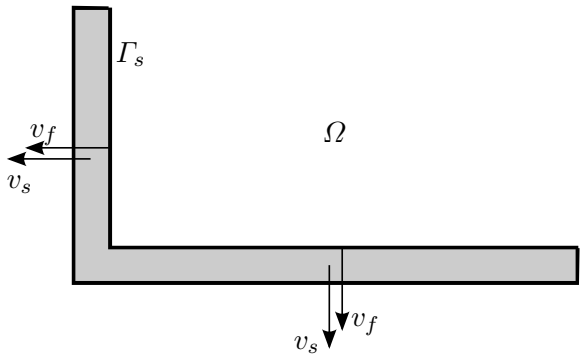

Figure 3.2: Definition of boundary conditions.

Y represents the boundary admittance, and the normal fluid particle velocity v_f is related to the normal derivative of the sound pressure p by means of the Euler equation in frequency domain

$$\hat{v}_f = -\frac{1}{\mathrm{i}\omega\varrho_0}\frac{\partial\hat{p}(\boldsymbol{x})}{\partial n(\boldsymbol{x})}. \tag{3.32}$$

The vector $\boldsymbol{n}(\boldsymbol{x})$ represents the outward normal at the surface point $\boldsymbol{x}$ and $\partial/\partial n(\boldsymbol{x})$ is the normal derivative.

In some cases, it is useful to consider Dirichlet boundary conditions. The Robin boundary condition as formulated in equation (3.31) is not suited for this case. Instead, we may use the Robin condition as an impedance boundary condition with the impedance $Z(\boldsymbol{x})$ as

$$Z(\boldsymbol{x})\left[v_f(\boldsymbol{x}) - v_s(\boldsymbol{x})\right] = p(\boldsymbol{x}) \qquad \text{and} \quad Z(\boldsymbol{x}) = \frac{1}{Y(\boldsymbol{x})}. \tag{3.33}$$

In case of a homogeneous Dirichlet boundary condition, the value of the impedance is zero and thus leading to $p(\boldsymbol{x}) = 0$. Obviously, the inhomogeneous Dirichlet condition results in $p(\boldsymbol{x}) = \bar{p}(\boldsymbol{x})$.

In the following we will prescribe boundary conditions as Neumann ($v_f(\boldsymbol{x}) = v_s(\boldsymbol{x}) = \bar{v}(\boldsymbol{x})$) and Dirichlet ($p(\boldsymbol{x}) = \bar{p}(\boldsymbol{x})$) conditions in both time and frequency domain.

3.2.2 The boundary value problem in time domain

The boundary $\Gamma \in \mathbb{R}^d$ is split up into two disjunct sub-boundaries, $\Gamma = \Gamma_p \cup \Gamma_v$. For Γ_p the pressure is given as an inhomogeneous Dirichlet condition

$$p(\boldsymbol{x}, t) = \bar{p}(\boldsymbol{x}, t) \qquad \boldsymbol{x} \in \Gamma_p, \quad t \geq 0 \tag{3.34}$$

and for Γ_v the normal component of particle velocity is prescribed as a Neumann condition

$$\boldsymbol{v}(\boldsymbol{x},t)\boldsymbol{n}(\boldsymbol{x}) = \bar{v}(\boldsymbol{x},t) \qquad \boldsymbol{x} \in \Gamma_v, \quad t \geq 0. \tag{3.35}$$

Making use of equation (3.14) the latter can be rewritten as

$$\frac{\partial \tilde{p}(\boldsymbol{x},t)}{\partial n} = -\varrho_0 \frac{\partial \bar{v}(\boldsymbol{x},t)}{\partial t} \qquad \boldsymbol{x} \in \Gamma_v, \quad t \geq 0 \tag{3.36}$$

where

$$\frac{\partial \tilde{p}(\boldsymbol{x},t)}{\partial n} = \boldsymbol{\nabla}\tilde{p}(\boldsymbol{x},t)\boldsymbol{n}(\boldsymbol{x}) \tag{3.37}$$

denotes the normal derivative of pressure.

In the domain Ω the wave equation (3.30) holds:

$$\Delta\tilde{p}(\boldsymbol{x},t) - \frac{1}{c^2}\frac{\partial^2 \tilde{p}(\boldsymbol{x},t)}{\partial t^2} = 0 \qquad \boldsymbol{x} \in \Omega, \quad t \geq 0. \tag{3.38}$$

In time domain the wave equation, the boundary conditions and the initial conditions should be satisfied by the solution pressure function. The initial conditions define the pressure and the particle velocity vector at the initial time $t = 0$

$$\begin{array}{rcl} p(\boldsymbol{x},0) & = & p^{(0)}(\boldsymbol{x}) \\ \boldsymbol{v}(\boldsymbol{x},0) & = & \boldsymbol{v}^{(0)}(\boldsymbol{x}) \end{array} \qquad \boldsymbol{x} \in \Omega. \tag{3.39}$$

3.2.3 The boundary value problem in frequency domain

The boundary value problem in frequency domain can be stated as follows. In each point of the domain Ω and for each frequency ω the Helmholtz equation holds:

$$\Delta\hat{p}(\boldsymbol{x}) + k^2\hat{p}(\boldsymbol{x}) = 0 \qquad \boldsymbol{x} \in \Omega \tag{3.40}$$

On the boundary Γ_p the complex amplitude of the sound pressure is prescribed as

$$\hat{p}(\boldsymbol{x},\omega) = \bar{p}(\boldsymbol{x},\omega) \qquad \boldsymbol{x} \in \Gamma_p. \tag{3.41}$$

On the boundary Γ_v the complex amplitude of the normal derivative of sound pressure is given:

$$\frac{\partial \hat{p}(\boldsymbol{x},\omega)}{\partial n} = -\mathrm{i}\omega\varrho_0\bar{\boldsymbol{v}}(\boldsymbol{x},\omega) \qquad \boldsymbol{x} \in \Gamma_v. \tag{3.42}$$

In frequency domain initial conditions can not be defined.

3.2.4 Weak form of the boundary value problem

The weak or variational form of the boundary value problem is the basis of the discretization technique used in the finite element method. The variational form assumes that the Helmholtz-equation (3.29) is satisfied in a weak sense, which means that for an arbitrary test function $\phi(\boldsymbol{x})$ over the domain Ω the following holds

$$\int_{\Omega} \phi(\boldsymbol{x}) \left(\boldsymbol{\nabla}^2 \hat{p}(\boldsymbol{x}) + k^2 \hat{p}(\boldsymbol{x}) \right) \mathrm{d}\boldsymbol{x} = 0. \tag{3.43}$$

From differentiation rule of product of functions (namely, that $(fg)' = f'g + fg'$) we get the following attribute of the $\boldsymbol{\nabla}$ operator:

$$\boldsymbol{\nabla} \cdot (\phi(\boldsymbol{x}) \boldsymbol{\nabla} \hat{p}(\boldsymbol{x})) = \boldsymbol{\nabla} \phi(\boldsymbol{x}) \boldsymbol{\nabla} \hat{p}(\boldsymbol{x}) + \phi(\boldsymbol{x}) \boldsymbol{\nabla}^2 \hat{p}(\boldsymbol{x}). \tag{3.44}$$

Substituting this into the weak form and splitting the integral, equation (3.43) can be rewritten as

$$\int_{\Omega} \boldsymbol{\nabla} \phi(\boldsymbol{x}) \boldsymbol{\nabla} \hat{p}(\boldsymbol{x}) \mathrm{d}\boldsymbol{x} - k^2 \int_{\Omega} \phi(\boldsymbol{x}) \hat{p}(\boldsymbol{x}) \mathrm{d}\boldsymbol{x} = \int_{\Omega} \boldsymbol{\nabla} \cdot (\phi(\boldsymbol{x}) \boldsymbol{\nabla} \hat{p}(\boldsymbol{x})) \mathrm{d}\boldsymbol{x}. \tag{3.45}$$

The right hand side can be simplified applying Gauss' theorem

$$\int_{\Omega} \boldsymbol{\nabla} \phi(\boldsymbol{x}) \boldsymbol{\nabla} \hat{p}(\boldsymbol{x}) \mathrm{d}\boldsymbol{x} - k^2 \int_{\Omega} \phi(\boldsymbol{x}) \hat{p}(\boldsymbol{x}) \mathrm{d}\boldsymbol{x} = \int_{\Gamma} \phi(\boldsymbol{x}) \hat{p}'_n(\boldsymbol{x}) \mathrm{d}\boldsymbol{x}. \tag{3.46}$$

Multiplying by $\varrho_0 c^2$ and substituting from (3.42) yields

$$\varrho_0 c^2 \int_{\Omega} \boldsymbol{\nabla} \phi(\boldsymbol{x}) \boldsymbol{\nabla} \hat{p}(\boldsymbol{x}) \mathrm{d}\boldsymbol{x} - \omega^2 \varrho_0 \int_{\Omega} \phi(\boldsymbol{x}) \hat{p}(\boldsymbol{x}) \mathrm{d}\boldsymbol{x} = -\mathrm{i}\omega \varrho^2 c^2 \int_{\Gamma_v} \phi(\boldsymbol{x}) \bar{\boldsymbol{v}}(\boldsymbol{x}) \mathrm{d}\boldsymbol{x}. \tag{3.47}$$

This shape of the weak form of the frequency domain boundary value problem is the first base of the discretization technique used by the Finite Element Method.

Chapter 4

Numerical methods

This chapter gives a detailed discussion of numerical techniques in linear acoustics. The finite and boundary element method, which are used in a wide range, are examined. A coupled method is introduced as a combination of these two. Finally, perfectly matched layers are presented as an alternative way of modeling infinite domains by means of artificial boundaries.

The first computer implementations of the finite element method appeared in the '60s. From that time, numerical simulations are applied in wider and wider scope in many fields of computational physics. By means of today's computer technology, problems with tens of thousands of nodes and elements can be analyzed efficiently, which allows the examination of complex problems in high resolution.

The same notations will be used here, as in chapter 3. The notations that will be introduced are also accepted and used.

4.1 The Finite Element Method

4.1.1 Introduction

The finite element method is a numerical procedure that searches an approximate solution of the acoustic boundary value problem. The basis of the finite element method is the weak form, in the shape that is given in equation (3.47). The main steps of the solution are

1. discretization of the weak form, where the integrals of equation (3.47) are transformed into a linear combination of a finite number of unknown solution coefficients;

2. the solution of the resulting linear system of equations.

In the following these steps will be described in detail.

4.1.2 Discretization of the weak form

The weak form of the acoustic boundary value problem will be discretized as follows. The spatial variation of the sound pressure (or its complex amplitude in the frequency domain) is approximated using a finite number of shape functions as

$$\hat{p}(\boldsymbol{x}) \approx \sum_{j=1}^{n} N_j(\boldsymbol{x}) p_j, \tag{4.1}$$

where $N_j(\boldsymbol{x})$ denotes the j-th shape function defined over the domain Ω and p_j is the j-th solution coefficient. Equation (4.1) can be considered as searching for the approximate solution in an n-dimensional vector space of functions defined over the domain Ω. The vector space is stretched by the basis functions $N_j(\boldsymbol{x})$.

The shape function approximation can be expressed with matrix-vector notations as

$$\hat{p}(\boldsymbol{x}) \approx \mathbf{N}(\boldsymbol{x})\mathbf{p} = [N_1(\boldsymbol{x}) \quad N_2(\boldsymbol{x}) \quad \dots \quad N_n(\boldsymbol{x})] \begin{bmatrix} p_1 \\ p_2 \\ \vdots \\ p_n \end{bmatrix}, \tag{4.2}$$

where $\mathbf{N}(\boldsymbol{x})$ is the matrix of the basis functions and $\mathbf{p}$ represents the vector of the coefficients.

The gradient of the pressure is approximated as

$$\boldsymbol{\nabla}\hat{p}(\boldsymbol{x}) \approx \sum_{j=1}^{n} \boldsymbol{\nabla} N_j(\boldsymbol{x}) p_j = \boldsymbol{\nabla}\mathbf{N}(\boldsymbol{x})\mathbf{p}, \tag{4.3}$$

where $\boldsymbol{\nabla} N_j$ denotes the gradient vector of the shape function N_j, and the matrix $\boldsymbol{\nabla}\mathbf{N}$ is defined as

$$\boldsymbol{\nabla}\mathbf{N}(\boldsymbol{x}) = [\boldsymbol{\nabla} N_1 \quad \boldsymbol{\nabla} N_2 \quad \dots \quad \boldsymbol{\nabla} N_n] = \begin{bmatrix} \dfrac{\partial N_1}{\partial x_1} & \dfrac{\partial N_2}{\partial x_1} & \cdots & \dfrac{\partial N_n}{\partial x_1} \\ \vdots & \vdots & \ddots & \vdots \\ \dfrac{\partial N_1}{\partial x_d} & \dfrac{\partial N_2}{\partial x_d} & \cdots & \dfrac{\partial N_n}{\partial x_d} \end{bmatrix}. \tag{4.4}$$

A similar finite dimensional approximation of the test function $\phi(\boldsymbol{x})$ can be introduced. Using a Galerkin formalism, the test function and the solution function

are written in the same basis. This means that the test function is discretized using the shape functions N_j as:

$$\phi(\boldsymbol{x}) \approx \sum_{j=1}^{n} N_j(\boldsymbol{x})\phi_j = \mathbf{N}(\boldsymbol{x})\boldsymbol{\phi}, \tag{4.5}$$

where

$$\boldsymbol{\phi} = \{\phi_1 \quad \phi_2 \quad \dots \quad \phi_n\}^T \tag{4.6}$$

is the vector of the test function coefficients. The approximation of the gradient of the test function is given as

$$\boldsymbol{\nabla}\phi(\boldsymbol{x}) \approx \sum_{j=1}^{n} \boldsymbol{\nabla}N_j(\boldsymbol{x})\phi_j = \boldsymbol{\nabla}\mathbf{N}(\boldsymbol{x})\boldsymbol{\phi}. \tag{4.7}$$

Substituting the approximations of the pressure, the test functions and their gradient vectors into equation (3.47) yields

$$\varrho_0 c^2 \int_\Omega \left(\boldsymbol{\nabla}\mathbf{N}(\boldsymbol{x})\boldsymbol{\phi}\right)^T \boldsymbol{\nabla}\mathbf{N}(\boldsymbol{x})\mathbf{p}\mathrm{d}\boldsymbol{x} - \omega^2\varrho_0 \int_\Omega \left(\mathbf{N}(\boldsymbol{x})\boldsymbol{\phi}\right)^T \mathbf{N}(\boldsymbol{x})\mathbf{p}\mathrm{d}\boldsymbol{x} = \\ = -\mathrm{i}\omega\varrho_0^2 c^2 \int_{\Gamma_v} \left(\mathbf{N}(\boldsymbol{x})\boldsymbol{\phi}\right)^T \bar{v}(\boldsymbol{x},\omega)\mathrm{d}\boldsymbol{x}. \tag{4.8}$$

Extracting the spatially constant terms from the integrals results in

$$\varrho_0 c^2 \boldsymbol{\phi}^T \int_\Omega \boldsymbol{\nabla}\mathbf{N}(\boldsymbol{x})^T \boldsymbol{\nabla}\mathbf{N}(\boldsymbol{x})\mathbf{p}\mathrm{d}\boldsymbol{x} - \omega^2\varrho_0 \boldsymbol{\phi}^T \int_\Omega \mathbf{N}(\boldsymbol{x})^T\mathbf{N}(\boldsymbol{x})\mathbf{p}\mathrm{d}\boldsymbol{x} = \\ = -\mathrm{i}\omega\varrho_0^2 c^2 \boldsymbol{\phi}^T \int_{\Gamma_v} \mathbf{N}(\boldsymbol{x})\bar{v}(\boldsymbol{x},\omega)\mathrm{d}\boldsymbol{x}. \tag{4.9}$$

As the variational form of the boundary value problem has to hold for any arbitrary test function $\phi(\boldsymbol{x})$, the test function coefficient vector $\boldsymbol{\phi}$ can be chosen arbitrarily in equation (4.9). Formally, this means that the vector $\boldsymbol{\phi}^T$ can be dropped from each term of the equation:

$$\varrho_0 c^2 \int_\Omega \boldsymbol{\nabla}\mathbf{N}(\boldsymbol{x})^T \boldsymbol{\nabla}\mathbf{N}(\boldsymbol{x})\mathbf{p}\mathrm{d}\boldsymbol{x} - \omega^2\varrho_0 \int_\Omega \mathbf{N}(\boldsymbol{x})^T\mathbf{N}(\boldsymbol{x})\mathbf{p}\mathrm{d}\boldsymbol{x} = \\ = -\mathrm{i}\omega\varrho_0^2 c^2 \int_{\Gamma_v} \mathbf{N}(\boldsymbol{x})\bar{v}(\boldsymbol{x},\omega)\mathrm{d}\boldsymbol{x}. \tag{4.10}$$

This is a system of linear equations for the unknown solution coefficients p_j. The system of equations can be expressed in a compact form as

$$\left(\mathbf{K} - \omega^2\mathbf{M}\right)\mathbf{p} = -\mathrm{i}\omega\mathbf{q}. \tag{4.11}$$

Herein $\mathbf{K}$ is the acoustic stiffness matrix defined as

$$\mathbf{K} = \varrho_0 c^2 \int_{\Omega} \boldsymbol{\nabla}\mathbf{N}(\boldsymbol{x})^T \boldsymbol{\nabla}\mathbf{N}(\boldsymbol{x}) \mathrm{d}\boldsymbol{x}, \tag{4.12}$$

$\mathbf{M}$ denotes the acoustic mass matrix

$$\mathbf{M} = \varrho_0 \int_{\Omega} \mathbf{N}(\boldsymbol{x})^T \mathbf{N}(\boldsymbol{x}) \mathrm{d}\boldsymbol{x}, \tag{4.13}$$

and the excitation vector $\mathbf{q}$ is described as

$$\mathbf{q} = \varrho_0^2 c^2 \int_{\Gamma_v} \mathbf{N}(\boldsymbol{x})^T \bar{v}(\boldsymbol{x}, \omega) \mathrm{d}\boldsymbol{x}. \tag{4.14}$$

If the velocity excitation $\bar{v}(\boldsymbol{x}, \omega)$ can be written as the superposition of the shape functions N_j, then the excitation vector can be expressed as

$$\mathbf{q} \approx \mathbf{A}\mathbf{v}_n, \tag{4.15}$$

where $\mathbf{A}$ is the acoustic excitation matrix formed as

$$\mathbf{A} = \varrho_0^2 c^2 \int_{\Gamma_v} \mathbf{N}(\boldsymbol{x})^T \mathbf{N}(\boldsymbol{x}) \mathrm{d}\boldsymbol{x}. \tag{4.16}$$

4.1.3 Element mass and stiffness matrices

For the case of an arbitrary three-dimensional problem over the domain Ω, the definition of the shape functions $N_j(\boldsymbol{x})$ would be a difficult task. Therefore, in a conventional finite element implementation, the selection of the basis functions is performed with a simultaneous approximating discretization of the problem domain Ω. The geometry, as can be seen in figure (4.1), is split up into a finite number of non-overlapping elements

$$\Omega \approx \bigcup_{e=1}^{N_e} \Omega_e. \tag{4.17}$$

The discrete geometry points that span the elements are called nodes and the whole discretized geometry (all nodes and elements) is called mesh.

The solution is approximated over each element using a small number of polynomial functions. As the integral over the domain Ω can be written as the sum of integrals over the element domains, the mass $\mathbf{M}$ and the stiffness $\mathbf{K}$ matrices can be expressed as a sum of element mass $\mathbf{M}_e$ and element stiffness $\mathbf{K}_e$ matrices. These element matrices are expressed as described in equations (4.12) and (4.13), but the integrals are performed over the element domains.

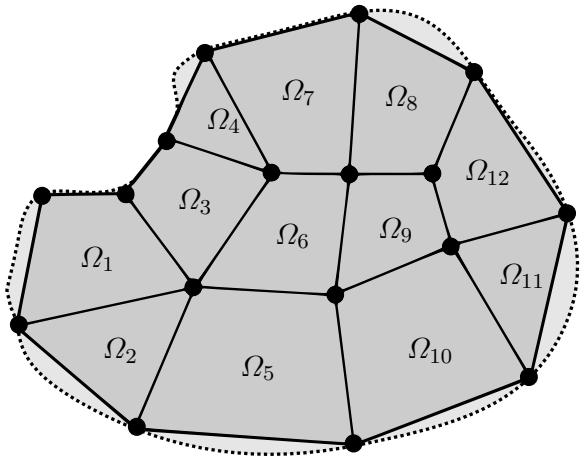

Figure 4.1: Geometry discretization of the finite element method

To be able to do this, a mapping coordinate transform needs to be introduced, that defines the the mapping between the location $\boldsymbol{\xi}$ in the standard element domain $\mathcal{O}_e$ and the location $\boldsymbol{x}$ in the element Ω_e. This can be done by applying geometry shape functions L_j, which define an interpolation between the nodal coordinates.

The sense of the mapping transformation is that the integrals over the element domains are performed over the standard element domain $\mathcal{O}_e$. This implies that the Jacobian matrix $\mathbf{J}$ of the mapping transformation needs to be constructed.

For the sake of convenience, the shape functions N_j can also be defined over the standard element domain $\mathcal{O}_e$, using $\boldsymbol{\xi}$ as the variables. The interpolation of the sound pressure can be written as

$$p(\boldsymbol{x}(\boldsymbol{\xi})) \approx \sum_{j=1}^{n} N_j(\boldsymbol{\xi}) p(\boldsymbol{x}_j), \qquad \boldsymbol{\xi} \in \mathcal{O}_e. \tag{4.18}$$

With this notation the element mass matrix can be expressed as

$$\mathbf{M}_e = \varrho_0 \int_{\mathcal{O}_e} \mathbf{N}(\boldsymbol{\xi})^T \mathbf{N}(\boldsymbol{\xi}) |\mathbf{J}(\boldsymbol{\xi})| \mathrm{d}\boldsymbol{\xi}. \tag{4.19}$$

The element stiffness matrix can be formulated as

$$\begin{aligned} \mathbf{K}_e &= \varrho_0 c^2 \int_{\mathcal{O}_e} \boldsymbol{\nabla}_{\boldsymbol{\xi}} \mathbf{N}(\boldsymbol{\xi})^T \mathbf{J}(\boldsymbol{\xi})^{-1} \left(\mathbf{J}(\boldsymbol{x})^T\right)^{-1} \boldsymbol{\nabla}_{\boldsymbol{\xi}} \mathbf{N}(\boldsymbol{\xi}) |\mathbf{J}(\boldsymbol{\xi})| \mathrm{d}\boldsymbol{\xi} = \\ &= \varrho_0 c^2 \int_{\mathcal{O}_e} \boldsymbol{\nabla}_{\boldsymbol{\xi}} \mathbf{N}(\boldsymbol{\xi})^T \left(\mathbf{J}(\boldsymbol{\xi})^T \mathbf{J}(\boldsymbol{x})\right)^{-1} \boldsymbol{\nabla}_{\boldsymbol{\xi}} \mathbf{N}(\boldsymbol{\xi}) |\mathbf{J}(\boldsymbol{\xi})| \mathrm{d}\boldsymbol{\xi}, \end{aligned} \tag{4.20}$$

where $\boldsymbol{\nabla}_{\boldsymbol{\xi}}$ denotes the $\boldsymbol{\nabla}$ operator with the standard element domain coordinates.

The detailed deduction and evaluation of the element mass and stiffness matrices for various element types can be found in [13]. The construction of a line element will be presented here as an example. As the results of these calculations will be used in section 4.4, the evaluation of the matrix elements will be described in detail.

4.1.4 Construction of the line element

The line element is the simplest element that can be used in the finite element method. It is not relevant in real applications, since most problems in acoustics involve a 3D domain. Even though, the evaluation of the element matrices can be demonstrated on it because of the simplicity of the calculation. Furthermore, the steps of the computation are the same for more complex elements.

The element geometry is defined by the coordinates of the two end nodes of the line, and the pressure distribution is defined by the pressure samples at the two ends. The standard element occupies the domain

$$\mathcal{O}_e = \{\xi | -1 \leq \xi \leq 1\}\,. \tag{4.21}$$

The geometry and pressure shape functions are identical ($L_j = N_j$):

$$\mathbf{L}(\xi) = \mathbf{N}(\xi) = \frac{1}{2}\left[1-\xi \quad 1+\xi\right]. \tag{4.22}$$

The gradient of the shape function is given as

$$\boldsymbol{\nabla}_{\boldsymbol{\xi}}\mathbf{L}(\xi) = \boldsymbol{\nabla}_{\boldsymbol{\xi}}\mathbf{N}(\xi) = \frac{1}{2}\left[-1 \quad 1\right]. \tag{4.23}$$

The Jacobian of the coordinate transform can be expressed as

$$\mathbf{J}(\xi) = (\boldsymbol{\nabla}_{\boldsymbol{\xi}}\mathbf{L}\mathbf{X})^T = \frac{1}{2}\left([-1 \quad 1]\begin{bmatrix} x_1 \\ x_2 \end{bmatrix}\right)^T = \frac{1}{2}(x_2 - x_1) = \frac{L}{2}, \tag{4.24}$$

where L denotes the length of the element. Clearly, the determinant of the matrix equals $L/2$. The expression of the element mass matrix is therefore given by

$$\begin{aligned}
\mathbf{M}_e &= \varrho_0 \int_{\mathcal{O}_e} \mathbf{N}(\xi)^T\mathbf{N}(\xi)|\mathbf{J}|\mathrm{d}\xi = \\
&= \frac{\varrho_0 L}{2^3}\int_{-1}^{1}\begin{bmatrix} 1-\xi \\ 1+\xi \end{bmatrix}[1-\xi \quad 1+\xi]\,\mathrm{d}\xi = \\
&= \frac{\varrho_0 L}{6}\begin{bmatrix} 2 & 1 \\ 1 & 2 \end{bmatrix}.
\end{aligned} \tag{4.25}$$

The sum of the elements of the mass matrix equals $\varrho_0 L$ that is the total mass of the line element.

The element stiffness matrix can be expressed using equation (4.20) as:

$$\begin{aligned}\mathbf{K}_e &= \frac{\varrho_0 c^2}{2^2}\int_{-1}^{1}\begin{bmatrix}-1\\1\end{bmatrix}(\mathbf{J}^T\mathbf{J})^{-1}[-1 \quad 1]|\mathbf{J}|\mathrm{d}\xi = \\ &= \frac{\varrho_0 c^2}{2^2}\int_{-1}^{1}|\mathbf{J}|\mathrm{d}\xi\begin{bmatrix}-1\\1\end{bmatrix}(\mathbf{J}^T\mathbf{J})^{-1}[-1 \quad 1] = \\ &= \frac{\varrho_0 c^2}{L}\begin{bmatrix}1 & -1\\-1 & 1\end{bmatrix}. \end{aligned} \tag{4.26}$$

4.2 The Boundary Element Method

4.2.1 The Helmholtz integral equation

The essential of the boundary element method (BEM) is that the acoustic variables can be calculated for any point of the domain if they are known on the boundary. The key to this method is the Helmholtz integral equation. Making use of Green's theorem, the integral equation will be deduced for an interior problem. Exterior problems will be regarded as degenerated cases of the interior ones by using the Sommerfeld radiation condition.

Interior problems

Green's theorem in the vector analysis states that the following holds for any closed domain Ω bounded by Γ and any $u(\boldsymbol{x})$ and $w(\boldsymbol{x})$ functions that are non-singular over Ω:

$$\begin{aligned}&\int_{\Omega}\left[u(\boldsymbol{x})\boldsymbol{\nabla}^2 w(\boldsymbol{x}) - w(\boldsymbol{x})\boldsymbol{\nabla}^2 u(\boldsymbol{x})\right]\mathrm{d}\boldsymbol{x} = \\ &\qquad = \int_{\Gamma}\left[u(\boldsymbol{x})\boldsymbol{\nabla} w(\boldsymbol{x}) - w(\boldsymbol{x})\boldsymbol{\nabla} u(\boldsymbol{x})\right]\boldsymbol{n}(\boldsymbol{x})\mathrm{d}\boldsymbol{x},\end{aligned} \tag{4.27}$$

where $\boldsymbol{n}(\boldsymbol{x})$ is the normal vector pointing outwards from Ω. Note, that for a normal pointing inwards, the right hand side of equation (4.27) changes its sign. Green's theorem can directly be derived from Gauss' theorem.

Let us apply Green's theorem as follows. Let $u(\boldsymbol{x}) = \hat{p}(\boldsymbol{x})$ and $w(\boldsymbol{x}) = g(\boldsymbol{x}, \boldsymbol{y})$, where $g(\boldsymbol{x}, \boldsymbol{y})$ is the Green's function for the considered acoustical problem. Green's function describes the sound pressure field of a point source placed at the given point $\boldsymbol{y}$ in a homogeneous acoustic field, i.e. it is the solution of equation

$$\left(\boldsymbol{\nabla}^2 + k^2\right) g(\boldsymbol{x}, \boldsymbol{y}) = -\delta(\boldsymbol{x} - \boldsymbol{y}), \tag{4.28}$$

where $\delta(\boldsymbol{x})$ is the Dirac-delta function. In a three dimensional space, Green's function is formed as

$$g(\boldsymbol{x}, \boldsymbol{y}) = \frac{1}{4\pi} \frac{\mathrm{e}^{-\mathrm{i}kr}}{r}, \tag{4.29}$$

where $r = |\boldsymbol{x} - \boldsymbol{y}|$.

Substitution into equation (4.27) yields:

$$\begin{aligned} \int_\Omega \left[\hat{p}(\boldsymbol{x})\boldsymbol{\nabla}^2 g(\boldsymbol{x}, \boldsymbol{y}) - g(\boldsymbol{x}, \boldsymbol{y})\boldsymbol{\nabla}^2 \hat{p}(\boldsymbol{x})\right] \mathrm{d}\boldsymbol{x} = \\ = \int_\Gamma \left[\hat{p}(\boldsymbol{x})\boldsymbol{\nabla} g(\boldsymbol{x}, \boldsymbol{y}) - g(\boldsymbol{x}, \boldsymbol{y})\boldsymbol{\nabla}\hat{p}(\boldsymbol{x})\right] \boldsymbol{n}(\boldsymbol{x}) \mathrm{d}\boldsymbol{x}. \end{aligned} \tag{4.30}$$

On the right hand side, the gradient of Green's function is needed. It is given in the three dimensional case as

$$\boldsymbol{\nabla} g(\boldsymbol{x}, \boldsymbol{y}) = -\mathrm{e}^{-\mathrm{i}kr} \frac{1 + \mathrm{i}kr}{r^2} \frac{\boldsymbol{r}}{r}, \tag{4.31}$$

where $\boldsymbol{r} = \boldsymbol{x} - \boldsymbol{y}$.

For the left hand side of equation (4.30) let us substitute $\boldsymbol{\nabla}^2 \hat{p}(\boldsymbol{x})$ with $-k^2 \hat{p}(\boldsymbol{x})$ from the Helmholtz equation (3.29), and making use of equation (4.28), $\boldsymbol{\nabla}^2 g(\boldsymbol{x}, \boldsymbol{y})$ can be replaced with $-\delta(\boldsymbol{x} - \boldsymbol{y}) - k^2 g(\boldsymbol{x}, \boldsymbol{y})$. We get

$$\begin{aligned} \int_\Omega \left[\hat{p}(\boldsymbol{x})(-\delta(\boldsymbol{x} - \boldsymbol{y}) - k^2 g(\boldsymbol{x}, \boldsymbol{y})) - g(\boldsymbol{x}, \boldsymbol{y})(-k^2)\hat{p}(\boldsymbol{x})\right] \mathrm{d}\boldsymbol{x} = \\ = \int_\Gamma \left[\hat{p}(\boldsymbol{x})\boldsymbol{\nabla} g(\boldsymbol{x}, \boldsymbol{y}) - g(\boldsymbol{x}, \boldsymbol{y})\boldsymbol{\nabla}\hat{p}(\boldsymbol{x})\right] \boldsymbol{n}(\boldsymbol{x}) \mathrm{d}\boldsymbol{x}. \end{aligned} \tag{4.32}$$

Simplifying the left hand side and multiplying the whole equation with -1 yields

$$\int_\Omega \hat{p}(\boldsymbol{x})\delta(\boldsymbol{x} - \boldsymbol{y}) \mathrm{d}\boldsymbol{x} = \int_\Gamma \left[g(\boldsymbol{x}, \boldsymbol{y})\boldsymbol{\nabla}\hat{p}(\boldsymbol{x}) - \hat{p}(\boldsymbol{x})\boldsymbol{\nabla} g(\boldsymbol{x}, \boldsymbol{y})\right] \boldsymbol{n}(\boldsymbol{x}) \mathrm{d}\boldsymbol{x}. \tag{4.33}$$

Using equation (3.28), the gradient of sound pressure can be substituted by the particle velocity. The scalar product of the gradient vector $\boldsymbol{\nabla} g(\boldsymbol{x}, \boldsymbol{y})$ and the normal vector $\boldsymbol{n}(\boldsymbol{x})$ is the normal derivative, $g'_n(\boldsymbol{x}, \boldsymbol{y})$ of Green's function. Similarly, the scalar product of the normal vector and the particle velocity vector $\hat{\boldsymbol{v}}(\boldsymbol{x})$ is the normal component of the particle velocity $\hat{v}_n$. Making use of these, equation (4.33) can be written as

$$\int_\Omega \hat{p}(\boldsymbol{x})\delta(\boldsymbol{x} - \boldsymbol{y}) \mathrm{d}\boldsymbol{x} = \int_\Gamma \left[-\mathrm{i}\omega\varrho_0 \hat{v}_n(\boldsymbol{x}) g(\boldsymbol{x}, \boldsymbol{y}) - \hat{p}(\boldsymbol{x}) g'_n(\boldsymbol{x}, \boldsymbol{y})\right] \mathrm{d}\boldsymbol{x}. \tag{4.34}$$

Further simplification can be achieved by taking into consideration the properties of the Dirac delta function. The integral on the right hand side can be expressed, dependent of the selection of y as

$$\int_{\Gamma} \left[-\mathrm{i}\omega\varrho_0\hat{v}_n(\boldsymbol{x})g(\boldsymbol{x},\boldsymbol{y}) - \hat{p}(\boldsymbol{x})g'_n(\boldsymbol{x},\boldsymbol{y})\right] \mathrm{d}\boldsymbol{x}. = \begin{cases} p(\boldsymbol{y}) & \text{if} \quad \boldsymbol{y} \in \Omega \\ p(\boldsymbol{y})/2 & \text{if} \quad \boldsymbol{y} \in \Gamma \\ 0 & \text{if} \quad \boldsymbol{y} \in \Omega_c \end{cases} \tag{4.35}$$

Equation (4.35) is the key of the Boundary Element Method as one can tell the sound pressure (i.e. $\hat{p}(\boldsymbol{x},\omega)$ for any ω) at any arbitrarily chosen point inside the domain $\boldsymbol{y}$ by the evaluation of the integral. This can be done if the sound pressure and the normal particle velocity is known on the boundary Γ.

Equations of (4.35) are called Helmholtz integral equations. These are equivalent to the Helmholtz equation (3.29) of the sound field, which means that their solution are the same for the same boundary conditions.

Exterior problems and the Sommerfeld radiation condition

Helmholtz integral equations can be applied to calculate the sound field in a closed domain. In case of an exterior problem the solution needs to be calculated in an unbounded, infinite domain. This infinite domain can be regarded as a degeneration of the finite domain case. Let Ω be bounded by Γ on the interior side, and bounded by a sphere-surface Γ_∞ with the radius of R on the exterior side, where R is infinitely large. This is shown in figure 4.2. Equation(4.35) can be formed for the combined surface $\Gamma \cup \Gamma_\infty$ as

$$\begin{aligned} \hat{p}(\boldsymbol{y}) = &\int_{\Gamma} \left[-\mathrm{i}\omega\varrho_0\hat{v}_n(\boldsymbol{x})g(\boldsymbol{x},\boldsymbol{y}) - \hat{p}(\boldsymbol{x})g'_n(\boldsymbol{x},\boldsymbol{y})\right] \mathrm{d}\boldsymbol{x} + \\ &+ \int_{\Gamma_\infty} \left[-\mathrm{i}\omega\varrho_0\hat{v}_n(\boldsymbol{x})g(\boldsymbol{x},\boldsymbol{y}) - \hat{p}(\boldsymbol{x})g'_n(\boldsymbol{x},\boldsymbol{y})\right] \mathrm{d}\boldsymbol{x}, \quad \text{if} \quad \boldsymbol{y} \in \Omega. \end{aligned} \tag{4.36}$$

For exterior problems the Sommerfeld radiation condition is used, namely that surface integral on Γ_∞ vanishes. This is equivalent to the statement that there are no reflected pressure waves from the unbounded, free field.

4.2.2 Discretization and solution

The discretization process of the integrals is done by means of shape functions similarly to the finite element method. Geometry discretization can be seen in figure 4.3. The approximated pressure and velocity is expressed as

$$\hat{p}(\boldsymbol{x}) \approx \sum_{j=1}^{n} N_j(\boldsymbol{x})p_j = \mathbf{N}(\boldsymbol{x})\mathbf{p}; \tag{4.37}$$

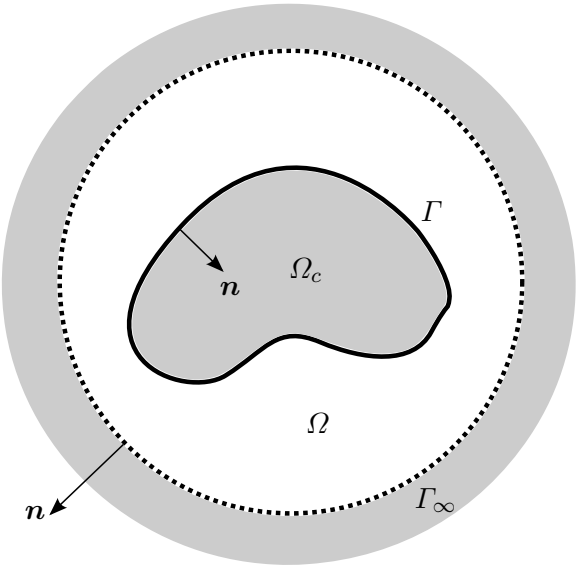

Figure 4.2: Exterior problem as a degeneration of an interior problem

$$\hat{v}_n(\boldsymbol{x}) \approx \sum_{j=1}^{n} N_j(\boldsymbol{x}) v_j = \mathbf{N}(\boldsymbol{x})\mathbf{v}. \tag{4.38}$$

Substituting these into equation (4.35), for the $\boldsymbol{y} \in \Omega$ case we get

$$\hat{p}(\boldsymbol{y}) = -\int_\Gamma \mathrm{i}\omega\varrho_0 \sum_{j=1}^{n} N(\boldsymbol{x}) g(\boldsymbol{x},\boldsymbol{y}) \mathrm{d}\boldsymbol{x} v_j - \int_\Gamma \sum_{j=1}^{n} N_j(\boldsymbol{x}) g'_n(\boldsymbol{x},\boldsymbol{y}) \mathrm{d}\boldsymbol{x} p_j. \tag{4.39}$$

Rearranging the sums and the integrals yields

$$\hat{p}(\boldsymbol{y}) = \sum_{j=1}^{n} a_j(\boldsymbol{y}) p_j - \sum_{j=1}^{n} b_j(\boldsymbol{y}) v_j, \tag{4.40}$$

where the coefficients

$$a_j(\boldsymbol{y}) = -\int_\Gamma N_j(\boldsymbol{x}) g'_n(\boldsymbol{x},\boldsymbol{y}) \mathrm{d}\boldsymbol{x}; \tag{4.41}$$

$$b_j(\boldsymbol{y}) = \mathrm{i}\omega\varrho_0 \int_\Gamma N_j(\boldsymbol{x}) g(\boldsymbol{x},\boldsymbol{y}) \mathrm{d}\boldsymbol{x}. \tag{4.42}$$

For the evaluation of equation (4.40) p_j and v_j must be known for all j. However, the problem definition prescribes the sound pressure or the normal particle

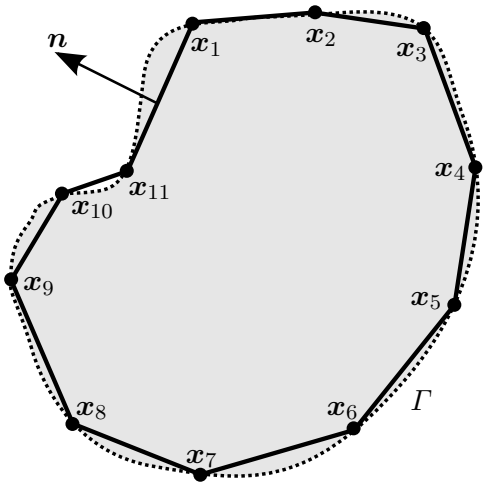

Figure 4.3: Discretization of the boundary surface

velocity on the boundary, but not both. Thus, the unknown values must be calculated first. This can be done as follows. Equation (4.35) should be written in similar discretized form as equation (4.40) for the $\boldsymbol{y} \in \Gamma$ case, and set up n independent, linear equations using the discretized form. For the q-th equation, let the surface point $\boldsymbol{y}$ be equal to the q-th node ($\boldsymbol{y} = \boldsymbol{x}_q$):

$$\frac{p_q}{2} = \sum_{j=1}^{n} a_j(\boldsymbol{x}_q) p_j - \sum_{j=1}^{n} b_j(\boldsymbol{x}_q) v_j, \qquad q = 1 \ldots n. \tag{4.43}$$

This can be written in matrix form as

$$\mathbf{A}\mathbf{p} = \mathbf{B}\mathbf{v}, \tag{4.44}$$

where the elements of $\mathbf{A}$ and $\mathbf{B}$ matrices are expressed as:

$$\begin{aligned} A_{qj} = a_j(\boldsymbol{x}_q) - \frac{\delta_{qj}}{2} &= -\int_{\Gamma} N_j(\boldsymbol{x}) g_n'(\boldsymbol{x}, \boldsymbol{y}) \mathrm{d}\boldsymbol{x} - \frac{\delta_{qj}}{2}; \\ B_{qj} = b_j(\boldsymbol{x}_q) &= \mathrm{i}\omega\varrho_0 \int_{\Gamma} N_j(\boldsymbol{x}) g(\boldsymbol{x}, \boldsymbol{y}) \mathrm{d}\boldsymbol{x}, \end{aligned} \tag{4.45}$$

δ_{qj} denoting the Kronecker delta, i.e. 1 if $q = j$ and 0 otherwise.

Equation (4.44) can be solved for any given combination of pressure or normal particle velocity boundary conditions. The solution produces both acoustical variables for all nodes of the surface. Making use of this, the sound pressure can be calculated for any point inside Ω. This method is also known as the direct boundary element method.

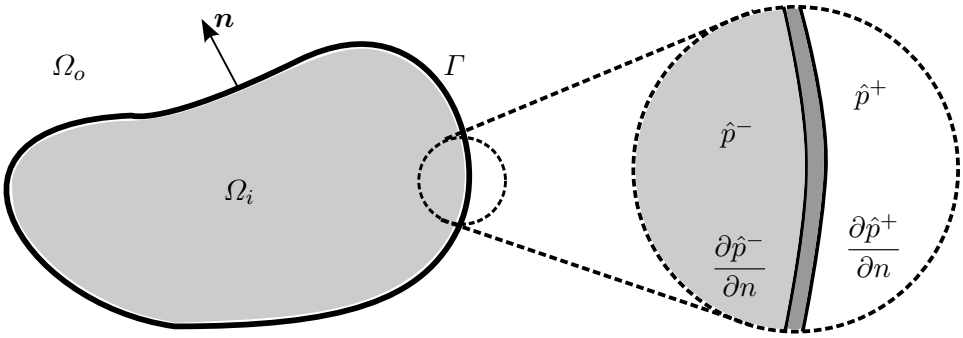

Figure 4.4: Definition of layer potentials in the indirect BEM

The matrices of equation (4.44) are frequency dependent full matrices. The frequency dependency means that they have to be recalculated for every distinct testing frequency. The fullness means that fast inverting methods for sparse matrices can not be applied here, in most cases Gauss elimination should be used. Hence, the boundary element method is not a reasonable substitution of the finite element method for interior problems.

4.2.3 The indirect boundary element method

The indirect boundary element method is able to solve the internal and external acoustic radiation and scattering problem simultaneously. The indirect representation uses layer potentials that are the differences between the outside and inside values of pressure and its normal derivative respectively, as can be seen in figure 4.4.

$$\begin{aligned} \mu &= \hat{p}^+ - \hat{p}^-; \\ \sigma &= \frac{\partial \hat{p}^+}{\partial n} - \frac{\partial \hat{p}^-}{\partial n}. \end{aligned} \tag{4.46}$$

μ is the difference between outside and inside pressure on the surface and is called the jump of pressure or the double layer potential, while σ is the difference between outside and inside normal derivatives on the surface and is called the jump of normal derivative of pressure or the single layer potential.

The acoustic variables at any point in the volume $\Omega = \Omega_i \cup \Omega_o$ are computed as a function of these two layer potentials. The boundary conditions can also be formulated in terms of the layer potentials.

The indirect form of the boundary element method will not be discussed here in more detail, as the steps of the formulation are not relevant for our further dis-

cussions. The formulation of the equations and deduction of the matrix form can be found in e.g. [10].

4.3 The coupled FE/BE method

The coupled FE/BE method is a combination of the finite element and the direct boundary element method and is able to solve the interior and exterior acoustic radiation and scattering problem, like the indirect BEM. The main difference is that the problem is solved here by means of FEM in the interior domain, while direct BEM is applied to set up boundary conditions.

4.3.1 Problem definition

The following acoustical problem, which is a generalization of the model that is used for organ pipe simulation, will be discussed here. A resonator object is placed into a free sound field with an acoustical point source in its vicinity. The sound pressure should be determined for the entire volume (both inside and outside the resonator).

The region of interest Ω is the union of the interior (Ω_i) and the exterior (Ω_o) domains. The interaction between the sound fields of these two regions is determined by the mechanical structure of the resonator and can be expressed by boundary conditions on the common boundary (Γ) of Ω_i and Ω_o. In the simplest case, the resonator object consists only of perfectly rigid walls and openings.

The evolving sound field, both for the interior and exterior domain, is a superposition of the incident ($\hat{p}_i$, $\hat{\boldsymbol{v}}_i$) field, and the reflected ($\hat{p}_r$, $\hat{\boldsymbol{v}}_r$) field. This means that the following holds for the whole domain:

$$\begin{array}{rcll} \hat{p}(\boldsymbol{x}) & = & \hat{p}_i(\boldsymbol{x}) + \hat{p}_r(\boldsymbol{x}); & \\ \hat{\boldsymbol{v}}(\boldsymbol{x}) & = & \hat{\boldsymbol{v}}_i(\boldsymbol{x}) + \hat{\boldsymbol{v}}_r(\boldsymbol{x}). & \end{array} \qquad \boldsymbol{x} \in \Omega \qquad (4.47)$$

4.3.2 Solution

The solution is carried out in the following steps.

1. Computation of the incident sound field.

2. Calculation of BE matrices ($\mathbf{A}$ and $\mathbf{B}$) to determine the relation of sound pressure and particle velocity for the reflected field on the boundary. Admittance boundary conditions can be set up expressed from these matrices.

3. Solving the interior problem with boundary conditions by means of FEM and evaluating the pressure field at any point of the exterior domain by the BEM.

4. Steps 1–3 have to be completed for each testing frequency. There are some simplification options that can be applied to speed up the process. These techniques will also be described in what follows.

The incident field

Acoustic variables of the incident field can directly be computed from the properties of the point source, by means of solving the inhomogeneous Helmholtz equation. The sound pressure field can be expressed, making use of equation (4.29) as

$$\hat{p}_i(\boldsymbol{x}) = \frac{p_s}{4\pi}\frac{\mathrm{e}^{-\mathrm{i}kr}}{r}, \tag{4.48}$$

where p_s is the amplitude of the point source and can be frequency dependent. The particle velocity can be determined using equation (3.29) and (4.31). We get

$$\hat{\boldsymbol{v}}_i(\boldsymbol{x}) = -\frac{p_s \mathrm{e}^{-\mathrm{i}kr}}{4\pi\varrho_0 c}\frac{1+\mathrm{i}kr}{r^2}\frac{\boldsymbol{r}}{r}. \tag{4.49}$$

Boundary conditions from the BEM

The reflected sound field is a solution of a radiation problem in a free sound field, hence the relation between its acoustic variables on the surface can be determined by means of the direct BEM as

$$\mathbf{A}\mathbf{p}_r = \mathbf{B}\mathbf{v}_r \tag{4.50}$$

The boundary of the resonator object can be split up into two domains.

1. Parts, where admittance boundary condition should be prescribed to compute the acoustic variables. Typically openings, where the interior and exterior domain is joined.

2. Parts, where the pressure or the normal particle velocity is given. For example a perfectly rigid wall, where $\hat{v}_n = 0$.

A simple example of splitting the surface is shown in figure 4.5. As seen, it is not necessary for the two domains to be coherent. Making use of this, the vectors

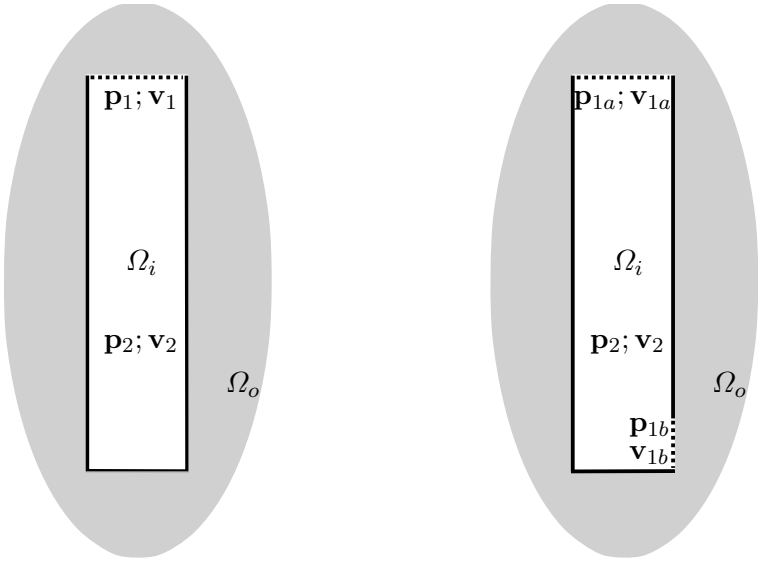

(a) one opening (b) two openings

Figure 4.5: Splitting of the boundary

of the pressure and velocity values at the nodes and the BEM matrices can also be split up as

$$\begin{bmatrix} \mathbf{A}_{11} & \mathbf{A}_{12} \\ \mathbf{A}_{21} & \mathbf{A}_{22} \end{bmatrix} \begin{bmatrix} \mathbf{p}_{r1} \\ \mathbf{p}_{r2} \end{bmatrix} = \begin{bmatrix} \mathbf{B}_{11} & \mathbf{B}_{12} \\ \mathbf{B}_{21} & \mathbf{B}_{22} \end{bmatrix} \begin{bmatrix} \mathbf{v}_{r1} \\ \mathbf{v}_{r2} \end{bmatrix}. \tag{4.51}$$

Equation (4.51) can be expanded as

$$\begin{aligned} \mathbf{A}_{11}\mathbf{p}_{r1} + \mathbf{A}_{12}\mathbf{p}_{r2} &= \mathbf{B}_{11}\mathbf{v}_{r1} + \mathbf{B}_{12}\mathbf{v}_{r2}; \\ \mathbf{A}_{21}\mathbf{p}_{r1} + \mathbf{A}_{22}\mathbf{p}_{r2} &= \mathbf{B}_{21}\mathbf{v}_{r1} + \mathbf{B}_{22}\mathbf{v}_{r2}. \end{aligned} \tag{4.52}$$

From the second equation of (4.52) $\mathbf{p}_{r2}$ can be expressed as

$$\mathbf{p}_{r2} = \mathbf{A}_{22}^{-1}\left(-\mathbf{A}_{21}\mathbf{p}_{r1} + \mathbf{B}_{21}\mathbf{v}_{r1} + \mathbf{B}_{22}\mathbf{v}_{r2}\right). \tag{4.53}$$

Substituting this into the first equation of (4.52) we get:

$$\begin{aligned} &\left(\mathbf{A}_{11} - \mathbf{A}_{12}\mathbf{A}_{22}^{-1}\mathbf{A}_{21}\right)\mathbf{p}_{r1} = \\ &\quad \left(\mathbf{B}_{11} - \mathbf{A}_{12}\mathbf{A}_{22}^{-1}\mathbf{B}_{21}\right)\mathbf{v}_{r1} + \left(\mathbf{B}_{12} - \mathbf{A}_{12}\mathbf{A}_{22}^{-1}\mathbf{B}_{22}\right)\mathbf{v}_{r2}. \end{aligned} \tag{4.54}$$

The coefficient matrix of $\mathbf{p}_{r1}$ on the left hand side is known as the Schur's complement form of the block matrix $\mathbf{A}$. Using the notation

$$\mathbf{A}_c = \mathbf{A}_{11} - \mathbf{A}_{12}\mathbf{A}_{22}^{-1}\mathbf{A}_{21}$$

$$\begin{aligned} \mathbf{B}_{c1} &= \mathbf{B}_{11} - \mathbf{A}_{12}\mathbf{A}_{22}^{-1}\mathbf{B}_{21} \\ \mathbf{B}_{c2} &= \mathbf{B}_{12} - \mathbf{A}_{12}\mathbf{A}_{22}^{-1}\mathbf{B}_{22} \end{aligned} \tag{4.55}$$

equation (4.54) can be written as

$$\mathbf{A}_c\mathbf{p}_{r1} = \mathbf{B}_{c1}\mathbf{v}_{r1} + \mathbf{B}_{c2}\mathbf{v}_{r2}. \tag{4.56}$$

Now $\mathbf{v}_{r1}$ can be expressed:

$$\mathbf{v}_{r1} = \mathbf{B}_{c1}^{-1}\left(\mathbf{A}_c\mathbf{p}_{r1} - \mathbf{B}_{c2}\mathbf{v}_{r2}\right). \tag{4.57}$$

This is an admittance condition being equivalent to a Robin boundary condition. Note that $\mathbf{v}_{r2}$ equals $-\mathbf{v}_{i2}$ if the structure is considered to be perfectly rigid.

Solving the FEM equation

The Helmholtz equation (3.29) is solved by the means of the finite element method in the interior domain. The equation can be written in matrix form similar to equation (4.11) as

$$\left(\mathbf{K} - \omega^2\mathbf{M}\right)\mathbf{p} = -\mathrm{i}\omega\mathbf{A}\mathbf{v}. \tag{4.58}$$

For simplicity, the following notation will be used

$$\begin{aligned} \mathbf{S} &= \mathbf{K} - \omega^2\mathbf{M}; \\ \mathbf{Q} &= -\mathrm{i}\omega\mathbf{A}. \end{aligned} \tag{4.59}$$

The discretized geometry of the interior domain can also be split up into two subdomains similarly as it was done for the surface. Equation (4.58) can be rewritten in the split form similar to equation (4.51) as

$$\begin{bmatrix} \mathbf{S}_{11} & \mathbf{S}_{12} \\ \mathbf{S}_{21} & \mathbf{S}_{22} \end{bmatrix} \begin{bmatrix} \mathbf{p}_{i1} + \mathbf{p}_{r1} \\ \mathbf{p}_{i2} + \mathbf{p}_{r2} \end{bmatrix} = \begin{bmatrix} \mathbf{Q}_{11} & \mathbf{Q}_{12} \\ \mathbf{Q}_{21} & \mathbf{Q}_{22} \end{bmatrix} \begin{bmatrix} \mathbf{v}_{i1} + \mathbf{v}_{r1} \\ \mathbf{v}_{i2} + \mathbf{v}_{r2} \end{bmatrix} \tag{4.60}$$

For further analysis we will consider the case when there is no excitation source in the interior domain, which yields $\mathbf{v}_2 = \mathbf{0}$. Then equation (4.60) can be formed as

$$\begin{bmatrix} \mathbf{S}_{11} & \mathbf{S}_{12} \\ \mathbf{S}_{21} & \mathbf{S}_{22} \end{bmatrix} \begin{bmatrix} \mathbf{p}_{i1} + \mathbf{p}_{r1} \\ \mathbf{p}_2 \end{bmatrix} = \begin{bmatrix} \mathbf{Q}_{11} & \mathbf{Q}_{12} \\ \mathbf{Q}_{21} & \mathbf{Q}_{22} \end{bmatrix} \begin{bmatrix} \mathbf{v}_{i1} + \mathbf{v}_{r1} \\ \mathbf{0} \end{bmatrix}. \tag{4.61}$$

Expanding the matrix equation we get:

$$\begin{aligned} \mathbf{S}_{11}(\mathbf{p}_{i1} + \mathbf{p}_{r1}) + \mathbf{S}_{12}(\mathbf{p}_{i2} + \mathbf{p}_{r2}) &= \mathbf{Q}_{11}(\mathbf{v}_{i1} + \mathbf{v}_{r1}) \\ \mathbf{S}_{21}(\mathbf{p}_{i1} + \mathbf{p}r1) + \mathbf{S}_{22}\mathbf{p}_2 &= \mathbf{Q}_{21}\mathbf{v}_1 \end{aligned} \tag{4.62}$$

Substituting $\mathbf{v}_{r1}$ from equation (4.57) into the second equation yields

$$\mathbf{S}_{21}(\mathbf{p}_{i1}+\mathbf{p}_{r1})+\mathbf{S}_{22}\mathbf{p}_2=\mathbf{Q}_{21}\Big[\mathbf{v}_{i1}+\mathbf{B}_{c1}^{-1}(\mathbf{A}_c\mathbf{p}_{r1}-\mathbf{B}_{c2}\mathbf{v}_{r2})\Big]. \tag{4.63}$$

Now $\mathbf{p}_2$ can be expressed:

$$\mathbf{p}_2=\mathbf{S}_{22}^{-1}\Big\{-\mathbf{S}_{21}(\mathbf{p}_{i1}+\mathbf{p}_{r1})+\mathbf{Q}_{21}\Big[\mathbf{v}_{i1}+\mathbf{B}_{c1}^{-1}(\mathbf{A}\mathbf{p}_{r1}-\mathbf{B}_{c2}\mathbf{v}_{r2})\Big]\Big\}. \tag{4.64}$$

Equation (4.64) can be substituted into the first equation of (4.62), which can be formed as

$$\begin{aligned}&\mathbf{S}_{11}(\mathbf{p}_{i1}+\mathbf{p}_{r1})+\\&+\mathbf{S}_{12}\Bigg(\mathbf{S}_{22}^{-1}\Big\{-\mathbf{S}_{21}(\mathbf{p}_{i1}+\mathbf{p}_{r1})+\mathbf{Q}_{21}\Big[\mathbf{v}_{i1}+\mathbf{B}_{c1}^{-1}(\mathbf{A}\mathbf{p}_{r1}-\mathbf{B}_{c2}\mathbf{v}_{r2})\Big]\Big\}\Bigg)\;=\\&=\mathbf{Q}_{11}(\mathbf{v}_{i1}+\mathbf{B}_{c1}^{-1}(\mathbf{A}_c\mathbf{p}_{r1}-\mathbf{B}_{c2}\mathbf{v}_{r2})).\end{aligned} \tag{4.65}$$

As $\mathbf{p}_{i1}$, $\mathbf{v}_{i1}$ and $\mathbf{v}_{r2}$ are known, $\mathbf{p}_{r1}$ can be expressed as

$$\begin{aligned}\mathbf{p}_{r1}=&\Big[\mathbf{S}_{11}-\mathbf{S}_{12}\mathbf{S}_{22}^{-1}\mathbf{S}_{21}+(\mathbf{S}_{12}\mathbf{S}_{22}^{-1}\mathbf{Q}_{21}-\mathbf{Q}_{11})\mathbf{B}_{c1}^{-1}\mathbf{A}\Big]^{-1}\cdot\\&\cdot\Big[-(\mathbf{S}_{11}-\mathbf{S}_{12}\mathbf{S}_{22}^{-1}\mathbf{S}_{21})\mathbf{p}_{i1}+(\mathbf{Q}_{11}-\mathbf{S}_{12}\mathbf{S}_{22}^{-1}\mathbf{Q}_{21})\mathbf{v}_{i1}-\\&-(\mathbf{Q}_{11}+\mathbf{S}_{12}\mathbf{S}_{22}^{-1}\mathbf{Q}_{21})\mathbf{B}_{c1}^{-1}\mathbf{B}_{c2}\mathbf{v}_{r2}\Big].\end{aligned} \tag{4.66}$$

By the evaluation of equation (4.66) the sound pressure can be calculated at nodes of the first type. The pressure can be evaluated for the rest of the interior domain by using the second equation of (4.62) as

$$\mathbf{p}_2=\mathbf{S}_{22}^{-1}(-\mathbf{S}_{21}\mathbf{p}_1+\mathbf{Q}_{21}\mathbf{v}_1). \tag{4.67}$$

Pressure field of the exterior domain can be calculated by means of the BEM. If the region of our interest is limited to the surface and the interior domain, this step can be skipped obviously.

4.3.3 Simplification options

To complete a solution, the pressure field of the region of interest must be computed for each testing frequency. This requires a large number of computational steps as equations (4.66) and (4.67) have to be evaluated, which may take quite some time if the resolution of the model is fine. To speed up the process there are some options that can be applied.

Firstly, the acoustic stiffness ($\mathbf{K}$) and mass ($\mathbf{M}$) matrices are independent of frequency, so they have to be calculated only once. Matrix $\mathbf{S}$ is frequency dependent, but can easily be generated by simple matrix addition from the matrices $\mathbf{K}$ and $\omega^2\mathbf{M}$. These matrices are sparse, which means that their storage size can be reduced and fast matrix inversion algorithms can be used on them.

The BEM matrices ($\mathbf{A}$ and $\mathbf{B}$) are frequency dependent dense (or full) matrices, but their values are varying slowly with respect to the frequency. The same holds for their Schur's complement forms ($\mathbf{A}_c$, $\mathbf{B}_{c1}$ and $\mathbf{B}_{c2}$). Making use of this, the computational process can be sped up by using interpolation formulae to approximate their values. Taking this into consideration it is sufficient to evaluate BEM matrices only for a few testing frequencies.

By these simplifications, the coupled method can be efficiently applied for the solution of a combined interior and exterior problem.

4.4 PML method

4.4.1 Computational absorbing boundaries

Many problems in acoustics, as well as in other fields of application like geophysics, oceanography and electro magnetics, involve waves in an unbounded medium. The solution of such problems using the finite element method or other domain-type methods usually requires the use of a finite computational domain in which the entire calculation is to be done. Thus, one has to introduce an artificial boundary that encloses the region of interest. To describe a well-posed mathematical problem in the finite computational domain, some boundary conditions must be imposed on the artificial boundary. There are various methods that can be applied for this problem, like classical infinite elements (see [3, 8, 12, 19]), low and high order boundary conditions (see [2, 15, 21, 27]) and absorbing layers (see [4, 7, 16]).

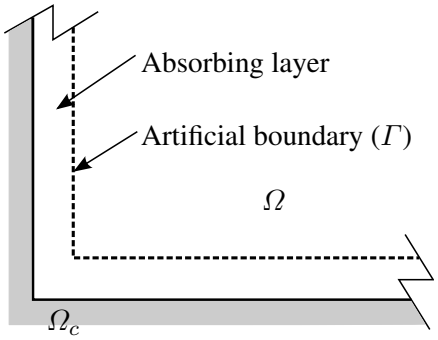

Figure 4.6: Setup of an absorbing layer

An absorbing layer is an artificial boundary layer, which is designed to damp or eliminate reflecting waves from the boundary of Ω. The setup of an absorbing layer can be seen in figure 4.6. The perfectly matched layer (PML) is a special absorbing boundary, that was invented by Bérenger in the mid 90's for electro magnetic problems (see [6]). It is equipped with two basic properties:

- It is designed to have *zero reflection* at the interface Γ for *any* plane wave;
- It is designed to make the solution *decay exponentially* inside the layer.

These two properties ensure excellent wave absorbance, at least on the continuous level. A wave outgoing from Ω enters the layer without any reflection, and then decays exponentially. By the time it arrives at the outer boundary of the PML it is very weak. Then it maybe reflected back into the PML, it decays exponentially again, and by the time it reaches the interface Γ on its way back into Ω it is too weak to cause any damage.

It was shown (see [26] e.g.), that the PML can be implemented for acoustic problems. In the following the deduction of the acoustic PML will be presented. Starting from the modification of the wave equation the weak form and the finite element discretization process will be described.

4.4.2 Acoustic wave equation for the PML

The wave equation and the Helmholtz equation for the perfectly matched layer will be deduced similarly as the original equations were in chapter 3. From the linearized equations of the principle of conversation of mass and conversation of momentum the equations will be formulated by means of introducing a new operator that provides the damping.

The linearized form of the conversation of mass (3.13) and the conversation of momentum (3.14) are given as

$$\left.\begin{aligned} \frac{\partial \tilde{\varrho}}{\partial t} + \varrho_0 \boldsymbol{\nabla} \cdot \tilde{\boldsymbol{v}} &= 0; \\ \varrho_0 \frac{\partial \tilde{\boldsymbol{v}}}{\partial t} + \boldsymbol{\nabla} \tilde{p} &= 0. \end{aligned}\right\} \tag{4.68}$$

By substituting the fluctuation of sound pressure instead of fluctuation of density, making use of the relation given in equation (3.15), we get

$$\left.\begin{aligned} \frac{1}{c^2} \frac{\partial \tilde{p}}{\partial t} + \varrho_0 \boldsymbol{\nabla} \cdot \tilde{\boldsymbol{v}} &= 0; \\ \varrho_0 \frac{\partial \tilde{\boldsymbol{v}}}{\partial t} + \boldsymbol{\nabla} \tilde{p} &= 0. \end{aligned}\right\} \tag{4.69}$$

Applying Fourier transform – as defined in equations (3.25) and (3.26) – the equations are transformed into the frequency domain and written as

$$\left.\begin{aligned} \frac{1}{c^2}\mathrm{i}\omega\hat{p} + \varrho_0 \boldsymbol{\nabla}\cdot\hat{\boldsymbol{v}} &= 0; \\ \varrho_0 \mathrm{i}\omega\hat{\boldsymbol{v}} + \boldsymbol{\nabla}\hat{p} &= 0. \end{aligned}\right\} \tag{4.70}$$

The damping is introduced by substituting the derivative operators of equation (4.70) by a damping operator that multiplies the derivative by a complex factor, which has a frequency dependent imaginary part. This imaginary part ensures the exponential decaying inside the layer. It also can be understood as a complex stretching of the spatial coordinates. Now the damping operator is introduced as a substitution of operator $\boldsymbol{\nabla}$. The new operator, $\boldsymbol{\nabla}_{\boldsymbol{s}}$ is described as

$$\boldsymbol{\nabla}_{\boldsymbol{s}} = -\sum_{j=1}^{d} \mathbf{e}_j \frac{1}{S_j}\frac{\partial}{\partial x_j}, \tag{4.71}$$

where d is the number of dimensions, $\mathbf{e}_j$ is the unitary vector of j-th dimension, x_j are the coordinates and the coefficients S_j are given as

$$S_j = 1 + \mathrm{i}\frac{\sigma_j}{\omega}. \tag{4.72}$$

This way, the PML parameters σ_j determine the damping for the certain directions. In a 3-D case for example, if x_1 is the PML thickness direction, then typically $\sigma_2 = \sigma_3 = 0$ while $\sigma_1 = \sigma(x_1)$ is called the PML damping function, and is a smooth increasing function of x_1 (say the parabola $\sigma(x_1) = Ax_1^2$). Note, that in the case of $\forall j : \sigma_j = 0$ we get the original operator $\boldsymbol{\nabla}$ back.

Substituting $\boldsymbol{\nabla}$ with the new operator $\boldsymbol{\nabla}_{\boldsymbol{s}}$ equation (4.70) is written as

$$\left.\begin{aligned} \frac{1}{c^2}\mathrm{i}\omega\hat{p} + \varrho_0 \boldsymbol{\nabla}_{\boldsymbol{s}}\cdot\hat{\boldsymbol{v}} &= 0; \\ \varrho_0 \mathrm{i}\omega\hat{\boldsymbol{v}} + \boldsymbol{\nabla}_{\boldsymbol{s}}\hat{p} &= 0, \end{aligned}\right\} \tag{4.73}$$

which can be expanded as

$$\left.\begin{aligned} \frac{1}{c^2}\mathrm{i}\omega\hat{p} + \varrho_0 \sum_{j=1}^{d} \frac{1}{S_j}\frac{\partial \hat{v}_j}{\partial x_j} &= 0; \\ \varrho_0 \mathrm{i}\omega\hat{\boldsymbol{v}} + \sum_{j=1}^{d} e_j \frac{1}{S_j}\frac{\partial \hat{p}}{\partial x_j} &= 0. \end{aligned}\right\} \tag{4.74}$$

By introducing new variables $\hat{p}^{(j)}$

$$\hat{p} = \sum_{j=1}^{d} \hat{p}^{(j)}, \tag{4.75}$$

equation (4.74) can be split up:

$$\left.\begin{aligned} \frac{1}{c^2}\mathrm{i}\omega\hat{p}^{(j)} + \varrho_0 \frac{1}{S_j}\frac{\partial \hat{v}_j}{\partial x_j} &= 0; \\ \varrho_0 \mathrm{i}\omega\hat{v}_j + \frac{1}{S_j}\frac{\partial \hat{p}}{\partial x_j} &= 0. \end{aligned}\right\} \tag{4.76}$$

Substituting the expression for S_j from equation (4.72) we get

$$\left.\begin{aligned} \frac{1}{c^2}(-\sigma_j + \mathrm{i}\omega)\hat{p}^{(j)} + \varrho_0 \frac{\partial \hat{v}_j}{\partial x_j} &= 0; \\ \varrho_0(-\sigma_j + \mathrm{i}\omega)\hat{v}_j + \frac{\partial \hat{p}}{\partial x_j} &= 0. \end{aligned}\right\} \tag{4.77}$$

Returning into the time domain by means of inverse Fourier transform – as defined in equation (3.26) – we get the governing equations of the PML in time domain given as $2d$ equations (for the $2d$ unknowns $p^{(j)}$ and $v^{(j)}$), as the following holds for $j = 1; 2; \ldots d$:

$$\left.\begin{aligned} \frac{1}{c^2}\frac{\partial p^{(j)}}{\partial t} - \frac{\sigma_j}{c^2}p^{(j)} + \varrho_0 \frac{\partial \hat{v}_j}{\partial x_j} &= 0; \\ \varrho_0 \frac{\partial v_j}{\partial t} - \varrho_0 \sigma_j v_j + \frac{\partial p}{\partial x_j} &= 0. \end{aligned}\right\} \tag{4.78}$$

The equations in the frequency domain can be derived from equation (4.73). Multiplying the first equation by $\mathrm{i}\omega$ and applying operator $\boldsymbol{\nabla_s}$ on the second equation we get

$$\left.\begin{aligned} \frac{1}{c^2}(\mathrm{i}\omega)^2\hat{p} + \varrho_0 \mathrm{i}\omega \boldsymbol{\nabla_s} \cdot \hat{\boldsymbol{v}} &= 0; \\ \varrho_0 \mathrm{i}\omega \boldsymbol{\nabla_s} \cdot \hat{\boldsymbol{v}} + \boldsymbol{\nabla_s}^2 \hat{p} &= 0. \end{aligned}\right\} \tag{4.79}$$

The second equation of (4.79) can be written as

$$\varrho_0 \mathrm{i}\omega \boldsymbol{\nabla_s} \cdot \hat{\boldsymbol{v}} = -\boldsymbol{\nabla_s}^2 \hat{p}. \tag{4.80}$$

Substituting equation (4.80) into the first equation of (4.79), the latter will be formed as

$$\frac{1}{c^2}(\mathrm{i}\omega)^2\hat{p} - \boldsymbol{\nabla}_{\boldsymbol{s}}^2\hat{p} = 0. \tag{4.81}$$

Making use of the definition of the wave number, $k = \omega/c$ and that $\mathrm{i}^2 = -1$, we get the Helmholtz equation for the PML, also known as the anisotropic Helmholtz equation, which is given as one single equation

$$\boldsymbol{\nabla}_{\boldsymbol{s}}^2\hat{p} + k^2\hat{p} = 0, \tag{4.82}$$

or in expanded form:

$$\sum_{j=1}^{d}\left(\frac{\omega}{\omega + \mathrm{i}\sigma_j}\right)^2 \hat{p} + k^2\hat{p} = 0. \tag{4.83}$$

Compare equation (4.82) to the linear Helmholtz equation (3.29):

$$\boldsymbol{\nabla}^2\hat{p} + k^2\hat{p} = 0. \tag{4.84}$$

As seen, in the frequency domain, the governing equation of the PML can easily be derived from the Helmholtz equation, by substituting $\boldsymbol{\nabla}$ with $\boldsymbol{\nabla}_{\boldsymbol{s}}$. Thus, the implementation of the PML in the frequency-dependent case is especially simple. The time domain analysis of the PML is also a field of recent research (see [11, 26]), but this is not examined herein. PML equations can also be formulated in other ways, see e.g. [7, 20, 30].

Note, that the damping factors σ_j in the modified operator $\boldsymbol{\nabla}_{\boldsymbol{s}}$ are dependent from $\boldsymbol{x}$. This yields that operator $\boldsymbol{\nabla}_{\boldsymbol{s}}$ itself is dependent from $\boldsymbol{x}$. This should be taken into consideration in the deduction of the weak form and at the discretization process.

The PML has the distinct advantage that on the continuous level it is 'perfect' by construction. Indeed it performs extremely well in many circumstances, especially for high-frequency waves. However there are still a number of PML-related issues that remain open and are a subject to current research. These include:

- While the PML is perfect on the continuous level, it is not perfect on the discrete level. In some cases the PML performs poorly when incorporated in a discrete model, especially in low frequencies. The PML seems to be more sensitive to discretization than the classical implementation of absorbing boundary conditions (see [15]). A good design of an ABC on the continuous level usually guarantees good performance on the discrete level; this does not seem to be the general case for PML.

- The performance of the PML is sensitive to the choice of the PML parameters, i.e. the PML thickness and the PML damping function $\sigma(x_j)$. For example, there is a clear trade-off in choosing the rate in which $\sigma(x_j)$ increases; on the one hand it should increase rapidly to generate sufficient damping, but on the other hand a rapid variation of $\sigma(x_j)$ requires a fine discretization with many elements inside the PML, which is inefficient.
- In some cases the basic PML may give rise to weak numerical instabilities. To a large extent these have been resolved, by modifying the basic formulation.

The PML can be formulated in other ways, as described in [7]. In the following a possible finite element implementation of the previously given formulation will be presented.

4.4.3 Weak form of the PML equation

For further analysis we will consider the PML problem given in the frequency domain. The weak form of the boundary value problem will be deduced similarly as it was for the isotropic Helmholtz equation (3.29).

Let us consider the introduced operator $\boldsymbol{\nabla_s}$ independent of $\boldsymbol{x}$ in the domain of Ω. This means that in the new operator the derivatives are multiplied by constants independent of $\boldsymbol{x}$. This way the weak form of equation (4.82) can be written as

$$\int_{\Omega} \phi(\boldsymbol{x}) \left(\boldsymbol{\nabla_s}^2 \hat{p}(\boldsymbol{x}) + k^2 \hat{p}(\boldsymbol{x}) \right) \mathrm{d}\boldsymbol{x} = 0. \tag{4.85}$$

It is trivial that rule (3.44) also holds for the operator $\boldsymbol{\nabla_s}$ as multiplying by constants does not make a change in the derivation rule. Equation (3.44) is given for $\boldsymbol{\nabla_s}$ simply as

$$\boldsymbol{\nabla_s} \cdot (\phi(\boldsymbol{x}) \boldsymbol{\nabla_s} \hat{p}(\boldsymbol{x})) = \boldsymbol{\nabla_s} \phi(\boldsymbol{x}) \boldsymbol{\nabla_s} \hat{p}(\boldsymbol{x}) + \phi(x) \boldsymbol{\nabla_s}^2 \hat{p}(\boldsymbol{x}). \tag{4.86}$$

Making use of this, by substituting into equation (4.85) we get

$$\int_{\Omega} \boldsymbol{\nabla_s} \phi(\boldsymbol{x}) \boldsymbol{\nabla_s} \hat{p}(\boldsymbol{x}) \mathrm{d}\boldsymbol{x} - k^2 \int_{\Omega} \phi(\boldsymbol{x}) \hat{p}(\boldsymbol{x}) \mathrm{d}\boldsymbol{x} = \int_{\Gamma_v} \boldsymbol{\nabla_s} \cdot (\phi(\boldsymbol{x}) \boldsymbol{\nabla_s} \hat{p}(\boldsymbol{x})) \, \mathrm{d}\boldsymbol{x}. \tag{4.87}$$

As in the case of the weak form of the isotropic Helmholtz equation (3.29), in the next step Gauss' theorem should be applied on the right side of equation (4.87). Gauss' (also known as divergence) theorem for the vector field $\boldsymbol{F}(\boldsymbol{x})$ is stated as

$$\int_{\Omega} \boldsymbol{\nabla} \cdot \boldsymbol{F}(\boldsymbol{x}) \mathrm{d}x = \int_{\Gamma} \boldsymbol{F}(\boldsymbol{x}) \cdot \boldsymbol{n}(\boldsymbol{x}) \mathrm{d}\boldsymbol{x}. \tag{4.88}$$

It should be considered, that how (4.88) can be rewritten for the operator $\boldsymbol{\nabla_s}$. Note, that we will make use of that the operator $\boldsymbol{\nabla_s}$ is considered independent of $\boldsymbol{x}$ in the domain Ω.

$$\int_\Omega \boldsymbol{\nabla_s} \cdot \boldsymbol{F}(\boldsymbol{x}) \mathrm{d}\boldsymbol{x} = \int_\Omega \left(\sum_{j=1}^{d} \mathbf{e}_j c_j \frac{\partial}{\partial x_j} \right) \cdot \left(\sum_{j=1}^{d} \mathbf{e}_j F_j \right) \mathrm{d}\boldsymbol{x} =$$

$$= \int_\Omega \boldsymbol{\nabla} \cdot \left(\sum_{j=1}^{d} \mathbf{e}_j c_j F_j \right) = \int_\Gamma F^{(c)} \cdot \boldsymbol{n}(\boldsymbol{x}) \mathrm{d}\boldsymbol{x}, \tag{4.89}$$

Where $\boldsymbol{F}^{(c)}$ represents in the three dimensional case, e.g.

$$\boldsymbol{F}^{(c)} = \begin{pmatrix} c_1 F_x \\ c_2 F_y \\ c_3 F_z \end{pmatrix}; \qquad \text{and} \qquad c_j = \frac{\omega}{\omega + i\sigma_j}. \tag{4.90}$$

Substituting this into equation (4.87) yields

$$\int_\Omega \boldsymbol{\nabla_s} \phi(\boldsymbol{x}) \boldsymbol{\nabla_s} \hat{p}(\boldsymbol{x}) \mathrm{d}\boldsymbol{x} - k^2 \int_\Omega \phi(\boldsymbol{x}) \hat{p}(\boldsymbol{x}) \mathrm{d}\boldsymbol{x} = \int_{\Gamma_v} \left[\phi(\boldsymbol{x}) \boldsymbol{\nabla_s} \hat{p}(\boldsymbol{x}) \right]^{(c)} \cdot \boldsymbol{n}(\boldsymbol{x}) \mathrm{d}\boldsymbol{x}. \tag{4.91}$$

From the Euler equation for the PML (second equation of (4.73)) the gradient of pressure can be expressed with the particle velocity as

$$\boldsymbol{\nabla_s} \hat{p} = -\varrho_0 \mathrm{i}\omega \hat{\boldsymbol{v}}. \tag{4.92}$$

Substituting from (4.92) into equation (4.91) we get

$$\int_\Omega \boldsymbol{\nabla_s} \phi(\boldsymbol{x}) \boldsymbol{\nabla_s} \hat{p}(\boldsymbol{x}) \mathrm{d}\boldsymbol{x} - k^2 \int_\Omega \phi(\boldsymbol{x}) \hat{p}(\boldsymbol{x}) \mathrm{d}\boldsymbol{x} = -\mathrm{i}\omega\varrho_0 \int_{\Gamma_v} \left[\phi(\boldsymbol{x}) \hat{\boldsymbol{v}}(\boldsymbol{x}) \right]^{(c)} \cdot \boldsymbol{n}(\boldsymbol{x}) \mathrm{d}\boldsymbol{x}. \tag{4.93}$$

Rearranging the right hand side and multiplying the whole equation by $\varrho_0 c^2$ we get the weak form of the boundary value problem for the PML in the final shape that will be used for the discretization process

$$\varrho_0 c^2 \int_\Omega \boldsymbol{\nabla_s} \phi(\boldsymbol{x}) \boldsymbol{\nabla_s} \hat{p}(\boldsymbol{x}) \mathrm{d}\boldsymbol{x} - \omega^2 \varrho_0 \int_\Omega \phi(\boldsymbol{x}) \hat{p}(\boldsymbol{x}) \mathrm{d}\boldsymbol{x} =$$

$$= -\mathrm{i}\omega \varrho_0^2 c^2 \int_{\Gamma_v} \phi(\boldsymbol{x}) \hat{\boldsymbol{v}}_n^{(c)}(\boldsymbol{x}) \mathrm{d}\boldsymbol{x}. \tag{4.94}$$

Here $\hat{\boldsymbol{v}}_n^{(c)}$ – similarly as the notations that were applied previously – can be described in the three dimensional case as

$$\hat{\boldsymbol{v}}_n^{(c)} = \begin{pmatrix} c_1 \hat{v}_x \\ c_2 \hat{v}_y \\ c_3 \hat{v}_z \end{pmatrix} \cdot \begin{pmatrix} n_1 \\ n_2 \\ n_3 \end{pmatrix} \qquad \text{and} \qquad c_j = \frac{\omega}{\omega + \mathrm{i}\sigma_j}. \tag{4.95}$$

In the following a finite element discretization of this weak form will be presented.

4.4.4 Discretization by the finite element method

Using similar approximations that were described in section 4.1 the following can be defined:

$$\begin{aligned}
\hat{p}(\boldsymbol{x}) &\approx \sum_{j=1}^{n} N_j(\boldsymbol{x}) p_j = \mathbf{N}(\boldsymbol{x})\mathbf{p}; \\
\boldsymbol{\nabla_s}\hat{p}(\boldsymbol{x}) &\approx \sum_{j=1}^{n} \boldsymbol{\nabla_s} N_j(\boldsymbol{x}) p_j = \boldsymbol{\nabla_s}\mathbf{N}(\boldsymbol{x})\mathbf{p}; \\
\phi(\boldsymbol{x}) &\approx \sum_{j=1}^{n} N_j(\boldsymbol{x}) \phi(j) = \mathbf{N}(\boldsymbol{x})\boldsymbol{\phi}; \\
\boldsymbol{\nabla_s}\phi(\boldsymbol{x}) &\approx \sum_{j=1}^{n} \boldsymbol{\nabla_s} N_j(\boldsymbol{x}) \phi_j = \boldsymbol{\nabla_s}\mathbf{N}(\boldsymbol{x})\boldsymbol{\phi}.
\end{aligned} \tag{4.96}$$

Substituting these into (4.94), and making use of that the equation holds for any test function $\phi(\boldsymbol{x})$ we get:

$$\begin{aligned}
\rho_0 c^2 \int_\Omega \boldsymbol{\nabla_s}\mathbf{N}(\boldsymbol{x})^T \boldsymbol{\nabla_s}\mathbf{N}(\boldsymbol{x})\mathbf{p}\mathrm{d}\boldsymbol{x} - \omega^2 \rho_0 \int_\Omega \mathbf{N}(\boldsymbol{x})^T \mathbf{N}(\boldsymbol{x})\mathbf{p}\mathrm{d}\boldsymbol{x} = \\
= -\mathrm{i}\omega\rho_0^2 c^2 \int_{\Gamma_v} \mathbf{N}(\boldsymbol{x})^T \hat{v}_n^{(c)}(\boldsymbol{x})\mathrm{d}\boldsymbol{x}.
\end{aligned} \tag{4.97}$$

The matrix form can be written as:

$$(\mathbf{K}_s - \omega^2 \mathbf{M}_s)\mathbf{p} = -\mathrm{i}\omega\mathbf{q}_s. \tag{4.98}$$

Where the matrices are expressed as:

$$\begin{aligned}
\mathbf{K}_s &= \rho_0 c^2 \int_\Omega \boldsymbol{\nabla_s}\mathbf{N}(\boldsymbol{x})^T \boldsymbol{\nabla_s}\mathbf{N}(\boldsymbol{x})\mathrm{d}\boldsymbol{x} \\
\mathbf{M}_s &= \rho_0 \int_\Omega \mathbf{N}(\boldsymbol{x})^T \mathbf{N}(\boldsymbol{x})\mathrm{d}\boldsymbol{x} \\
\mathbf{q}_s &= \rho_0^2 c^2 \int_{\Gamma_v} \mathbf{N}(\boldsymbol{x})^T \hat{v}_n^{(c)}(\boldsymbol{x})\mathrm{d}\boldsymbol{x}.
\end{aligned} \tag{4.99}$$

If the excitation can be expressed by the superposition of the shape functions then the excitation vector can be formed as:

$$\mathbf{q}_s = \mathbf{A}\mathbf{v}^{(c)}, \tag{4.100}$$

where

$$\mathbf{A} = \rho_0^2 c^2 \int_{\Gamma_v} \mathbf{N}(\boldsymbol{x})^T \mathbf{N}(\boldsymbol{x}) \mathrm{d}\boldsymbol{x} \tag{4.101}$$

Only the acoustic stiffness matrix and the excitation vector are changed compared to the original FEM matrices introduced in equations (4.12), (4.13) and (4.14). As usually there is no excitation prescribed for the damping elements, this means that only the stiffness matrix has to be recomputed if a normal acoustic element is changed into a damping element.

In this deduction, the value of the damping was considered independent of the location $\boldsymbol{x}$. However, the damping factor of elements can be set individually for each element. By this, a staggered damping function can be achieved.

4.4.5 Construction of the PML line element

The simplest element that can be constructed is a linear one dimensional element with two nodes. This example is not significant for real applications, but can be used efficiently for test experiments concerning the PML technique because of its simplicity.

Construction of the 1D, 2-node element can similarly be done as it were in the case of the classical line element. As the operator $\boldsymbol{\nabla}$ degenerates into derivation in the one dimensional case, the damping constant of operator $\boldsymbol{\nabla_s}$ can be extracted from the integral. The element mass and stiffness matrices can be formed, making use of equations (4.25) and (4.26), as:

$$\begin{aligned} \mathbf{M}_{e,s} &= \mathbf{M}_e = \frac{\varrho_0 L}{6} \begin{bmatrix} 2 & 1 \\ 1 & 2 \end{bmatrix}; \\ \mathbf{K}_{e,s} &= c_1^2 \mathbf{K}_e = c_1^2 \frac{\varrho_0 c^2}{L} \begin{bmatrix} 1 & -1 \\ -1 & 1 \end{bmatrix}, \end{aligned} \tag{4.102}$$

where

$$c_1 = \frac{\omega}{\omega + \mathrm{i}\sigma_1}. \tag{4.103}$$

As mentioned before, ω_1 can be chosen individually for each damping element. It is possible to regard the damping constants dependent of $\boldsymbol{x}$ inside the elements, but it should be taken into consideration, that it will be more difficult to evaluate the integrals. Two and three dimensional elements can also be derived from their original analogues.

As seen, element matrices of the damping elements are frequency dependent. This means, that in a finite element model the damping part of the system stiffness matrix $\mathbf{K}$ has to be recalculated for each testing frequency, and thus, modal solutions can not be used for the PML.

Chapter 5

Simulation technique and software

5.1 Measurement of the pipe transfer function

The measurement of the transfer function of an acoustic resonator is done in the following way. A vibration source is placed in the vicinity of the resonator object providing the excitation. Responses are measured by microphones at certain measurement locations. Transfer functions are computed by dividing the spectra of the responses by the excitation's spectrum.

In figure 5.1 the measurement setup of the pipe transfer function is shown. A loudspeaker is placed in the longitudinal axis of the pipe, creating a sound field, which excites the air column resonating in the pipe body. The excitation signal is a broadband signal, e.g. a logarithmic sweep sine function. Microphones are usually placed near the mouth of the pipe and at the open end. The signals of these microphones are analyzed by FFT analyzers. The whole setup is placed into an anechoic room, which provides the characteristics of a free sound field. The simulations are modeling this measurement setup.

In case of the simulation model, the organ pipe is given as a geometry mesh. The simplest case implies that the mesh consist of perfectly rigid, infinitely thin walls and openings. The rigidness of the walls means that the resonances of the mechanical structure of the pipe body are negligible, i.e. the resonating air does not produce vibrations in the walls. This yields that the normal component of the particle velocity is equivalent to zero on the walls. Note, that this is just an approximation, in the real case the walls and the air inside are in active interaction, which would require the analysis of a coupled structure and air vibration model. For the following, the walls are considered to be perfectly rigid.

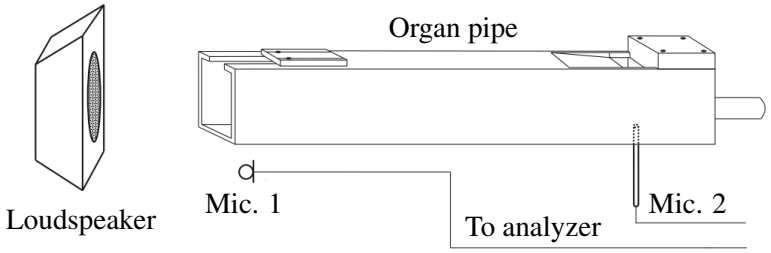

Figure 5.1: Setup of the transfer function measurement

The loudspeaker is simulated as a point source with given amplitude for each testing frequency, which is an acceptable approximation for the simulations. The microphones are substituted by simple measurement points, that can be placed anywhere in the domain of interest. Note, that in case of finite element simulations, for a measurement point that is not coincident with a node, the response can be calculated by means of interpolation, using the shape functions.

5.2 Mesh generation

The acoustic parameters of the organ sound are highly affected by the pipe's dimensions. Even small changes of the geometry can have major influence on the sounding and therefore, the discretization should be adequately fine. At the same time, by increasing the resolution of the model, storage size of the geometry and the computational effort will raise enormously.

The storage size of a mesh is proportional to the number of its nodes and elements. Hence in case of a surface geometry the storage size is $O(n^2)$, while for a volume geometry this value is $O(n^3)$, n denoting the average number of nodes in a unit length. As the system matrices are the size of $N \times N$ (where N represents the number of nodes), the storage size of these matrices ($\mathbf{A}$ and $\mathbf{B}$ for the BEM, $\mathbf{K}$ and $\mathbf{M}$ for the FEM) is $O(n^4)$ and $O(n^6)$, respectively. This means that the completion of a simulation of double discretization precision requires 64 times more storage size. Computational time will raise similarly, which means that a compromise must be made between the accuracy and the computational effort.

The validity range of the simulation is also dependent of the mesh resolution, the relation between the maximal element sizes (l_x, l_y and l_z) and the upper frequency limit ($f_{\max}$) is given as:

$$f_{\max} = \frac{c}{8 \max\{l_x, l_y, l_z\}}. \tag{5.1}$$

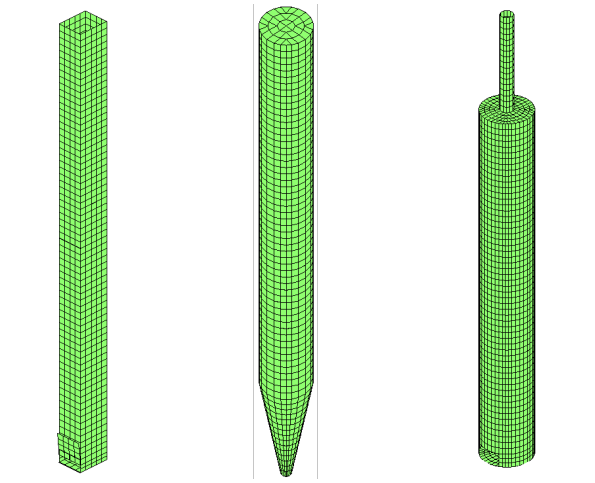

(a) Wooden pipe (b) Cylindric pipe (c) Chimney pipe

Figure 5.2: Meshes of different organ pipe types

It is useful to create a mesh that is discretized symmetrically and with uniform fineness. This way the values of l_x, l_y and l_z will be approximately equal, and effects of numerical instabilities caused by irregular meshing is minimized. The pipe meshes that were used for simulations were created by an algorithm that provides these attributes. Example meshes of different types of organ pipes can be seen in figure 5.2.

5.3 Application of numerical techniques

In the following it will be discussed that how can the presented numerical techniques be applied for organ pipe simulation and the determination of the pipe transfer function. The software packages that were used will also be presented here.

5.3.1 Simulations by the indirect BE method

In the case of the indirect BEM the region of our interest and thus, the sound field is split into an interior (inside the pipe) and an exterior (outside the pipe) domain. The connection and continuity between these two fields are described with boundary conditions, namely that the jump of pressure (the double layer potential) is zero at the boundaries (i.e. at the free edges of the mesh).

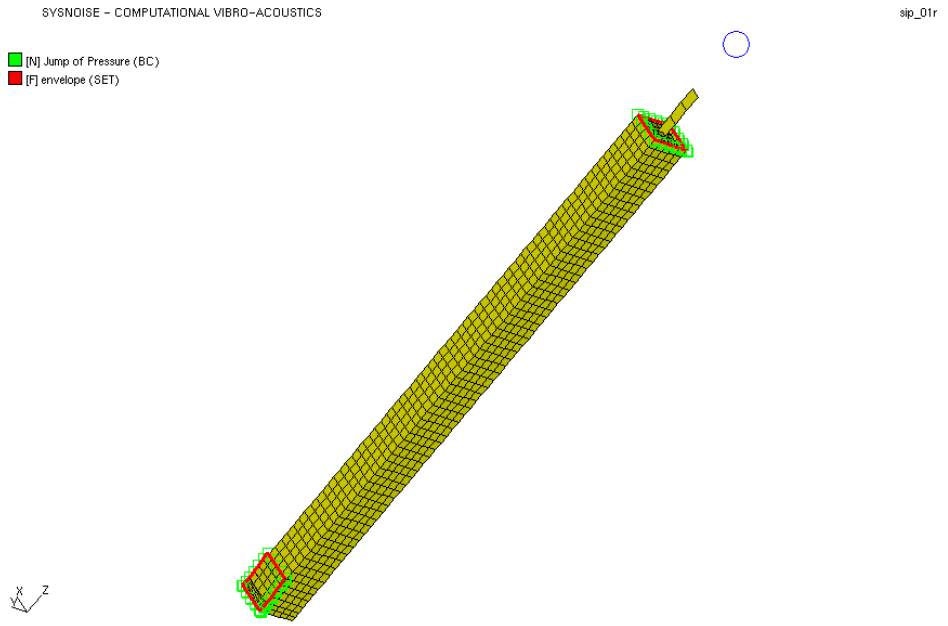

Figure 5.3: Simulation setup in the LMS Sysnoise software

The resonator geometry is given here as a surface geometry. The acoustic parameters at the measurement locations are computed for each testing frequency, one at a time.

The `LMS Sysnoise` software package was used for simulation tests involving the indirect BE method. The simulation setup screen is shown in figure 5.3. Red lines symbolize the free edges of the geometry, while the boundary conditions are shown in green. The blue circle indicates the point source. A field point mesh can be seen in the longitudinal axis of the pipe, its nodes are the measurement points.

5.3.2 Simulations by the coupled FE/BE method

The application of this method involves the usage of the FEM for the interior domain, and utilization of the BEM to calculate the boundary conditions. The mesh is given here as a volume geometry, but the surface geometry is also needed, to be able to apply the BEM. This way the storage size required by the mesh is somewhat bigger than in case of the indirect BEM.

When splitting up the boundary into openings and walls, the following problem

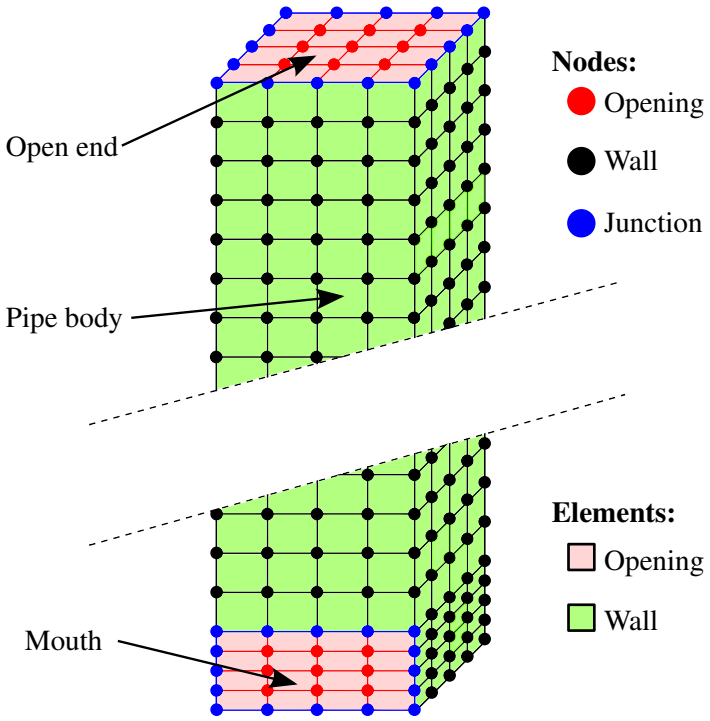

Figure 5.4: Mesh of a resonator of a wooden organ pipe

should be taken into consideration. As it is illustrated in figure 5.4, red nodes denote openings (mouth and open end), while black nodes represent walls. Blue nodes and lines symbolize the junctions these two. These nodes can either be regarded as red or black nodes, since the error of the discretization will vanish as the size of the elements becomes smaller. An other way to handle these junctions is to create two nodes for each blue node, a red and a black, with the same location and define their degrees of freedom respectively.

As the openings of the pipe consist of far less nodes than the walls, the Schur's complement technique can efficiently be used to set up the admittance boundary conditions for openings. Therefore, the frequency dependent part of the system matrices is relatively small compared to the size of the whole matrices. To speed up the computational process a spline interpolation formula were used on the admittance matrices, and thus, the BEM was only invoked for only a small fraction of the testing frequencies in case of pipe simulations. This resulted in a remarkable reduction of the computational time.

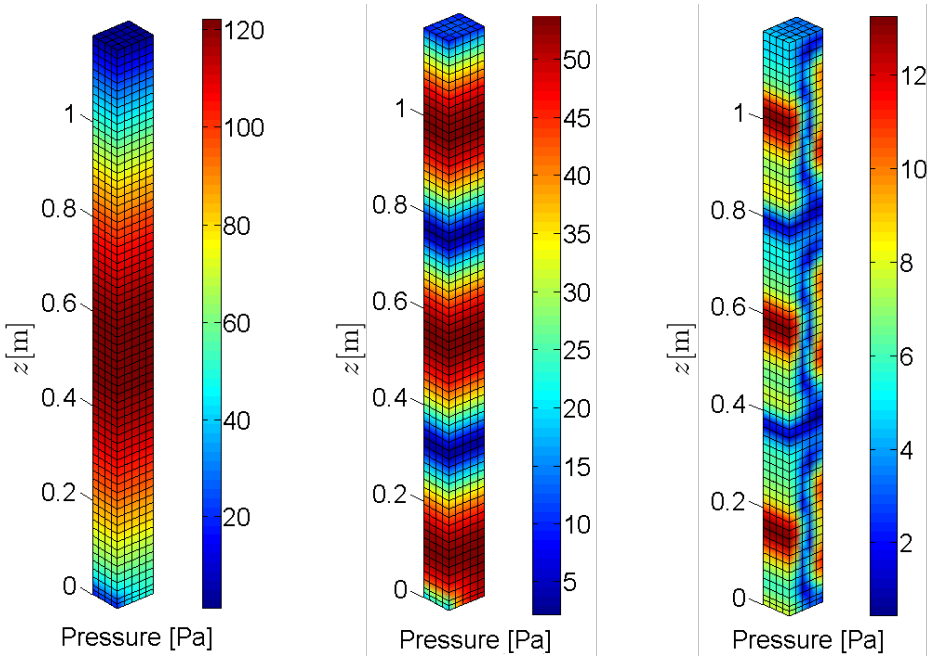

(a) 1st mode (b) 3rd mode (c) Combined mode

Figure 5.5: Pipe simulation in Matlab

Simulations involving the coupled FE/BE method were run using a solution program, developed by the author in `Matlab` language. The `AcouFEM` toolbox (see [13]) and the `AcouBEM` software were also used under the `Matlab` environment. All geometry meshes that were used for simulations (both indirect BEM and coupled FEM/BEM) were created by self-written scripts. Simulation plots can be seen in figure 5.5.

Chapter 6

Experiments and results

6.1 First steps: analytical calculations

The simplest analytic formula, which determines the eigenfrequencies of an air column resonating inside a tube with both ends open is the well known relation

$$f_n = 2n\frac{c}{4l}; \qquad n = 1; 2; 3 \ldots, \tag{6.1}$$

where f_n is the frequency of the n-th eigenmode, c is the speed of sound, and l denotes the length of the resonator. This means that an integer multiple of the half wavelengths of the longitudinal modes are equal to the length of the tube. For a tube with one end closed we get

$$f_n = (2n-1)\frac{c}{4l}; \qquad n = 1; 2; 3 \ldots. \tag{6.2}$$

Note, that these modes are the eigenfunctions of the wave equation with boundary conditions $p = 0$ at an open end and $v = 0$ at a closed end. As these conditions naturally does not apply in a real case, an end correction formula (see e.g. [18]) can be used to take the interaction between the interior and exterior field into consideration. This prescribes the effective length of the tube as

$$l_{\text{eff}} = l + 0.62r, \tag{6.3}$$

r denoting the radius of the tube. If both ends are open, the correction factor is doubled. The length correction effect for an organ pipe is shown in figure 6.1.

6.2 Validation simulations

As a validation of the model, simulations were run to compare analytical calculations and simulation results for several fictive cylindrical tube resonators. For

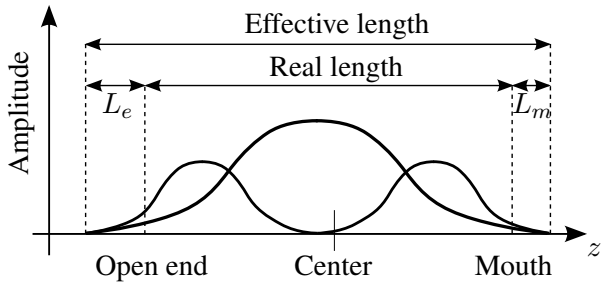

Figure 6.1: The length correction effect

Pipes with one end open						
Length [mm]	640			640		
Radius [mm]	32			48		
$l_{\mathbf{eff}}$ **[mm]**	660			670		
Harmonic	f_a [Hz]	f_s [Hz]	Stretch	f_a [Hz]	f_s [Hz]	Stretch
1. (Fund.)	130	129	1.000	128	127	1.000
2.	390	387	3.000	384	381	3.000
3.	650	648	5.023	640	640	5.039
4.	910	915	7.093	896	903	7.110
5.	1170	1185	9.186	1152	1174	9.244

Table 6.1: Comparison of results for pipes with one end open

what follows, the acoustic parameters $c = 343\ \frac{\mathrm{m}}{\mathrm{s}}$ as the speed of sound in air, and $\varrho_0 = 1.225\ \frac{\mathrm{kg}}{\mathrm{m}^3}$ as the average density of air will be used.

Simulation tests were run with the frequency resolution of 1 Hz, using the coupled FE/BE method. The frequencies of the harmonics and the simulated stretching according to the simulation results were compared. The stretching effect is represented by the stretching factor

$$\mathrm{Stretch} = \frac{f_n}{f_1}. \tag{6.4}$$

Test results are shown in table 6.1 and 6.2 for pipes with one end open and for pipes with an open end and a mouth opening, respectively. Figure 6.2 and 6.3 show comparison diagrams of simulation results.

As seen, results of validation simulations approximately match up with analytical calculations, deviations within a 2% range are epxerienced. The stretching values are higher for the wider pipes and resonance peaks are sharper for narrower pipes, as expected. The explanation of these effects is described in what follows.

Pipes with a mouth opening and an open end						
Length [mm]	1280			1280		
Radius [mm]	32			48		
l_{eff} **[mm]**	1320			1340		
Harmonic	f_a [Hz]	f_s [Hz]	Stretch	f_a [Hz]	f_s [Hz]	Stretch
1. (Fund.)	130	129	1.000	128	126	1.000
2. (Octave)	260	258	2.000	256	253	2.008
3.	390	388	3.008	384	381	3.024
4.	520	519	4.023	512	509	4.040
5.	650	650	5.039	640	638	5.063

Table 6.2: Comparison of results for pipes with a mouth opening and one open end

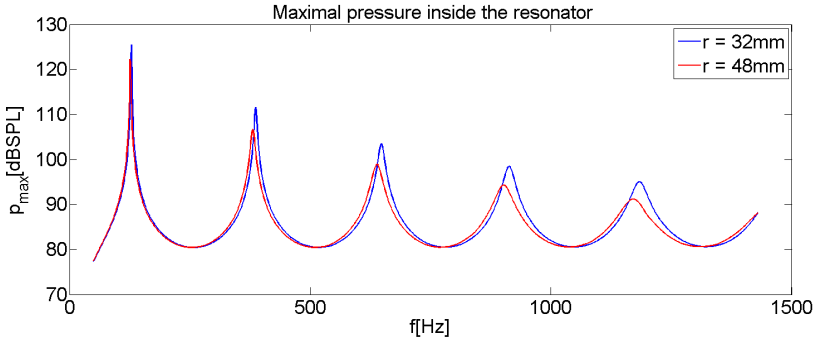

Figure 6.2: Simulation diagram of pipes with one end open

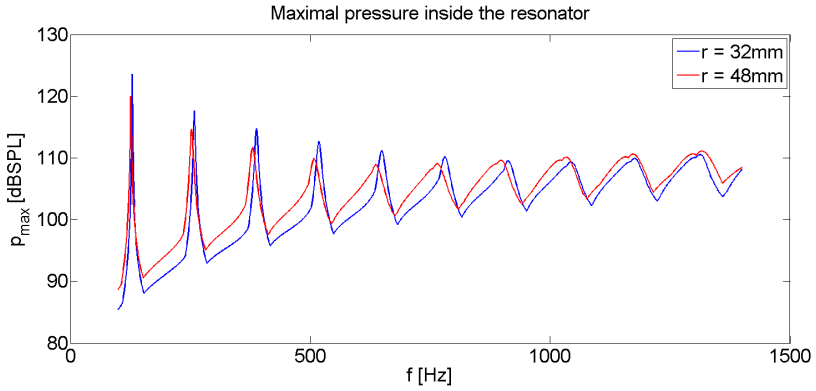

Figure 6.3: Simulation diagram of pipes with an open end and a mouth opening

6.3 Impedance analysis

Characteristics of the pipe transfer function and the organ sound itself can be understood by taking into consideration that the air column that resonates inside the pipe body is interacting with the exterior sound field.

The interaction between the interior and exterior sound field can be expressed by introducing terminating acoustic impedances at the enclosures of the pipes, i.e. the open end and the mouth. These impedances describe the load represented by the exterior sound field.

The radiation impedance in case of a plane piston moving in a long cylindric tube can be calculated analytically. In this case, the termination impedance can be described as an analogy of an electrical parallel R-L circuit (see: [5]). The equivalent acoustic circuit of concentrated parameters consists of an acoustic resistance and an acoustic mass. At high frequencies ($kr \gg 5$) the effect acoustic mass is negligible and the equivalent circuit is simplified to a pure acoustic resistance. The specific acoustic impedance of the termination is given as:

$$Z_s(\omega) = R_s \times \mathrm{i}\omega M_s = \frac{\mathrm{i}\omega R_s M_s}{R_s + \mathrm{i}\omega M_s}, \tag{6.5}$$

where

$$\left.\begin{array}{rcl} R_s & = & 1.505\varrho_0 c \\ M_s & = & 0.613 r \varrho_0 \end{array}\right\} \qquad \text{if} \qquad kr < 5; \tag{6.6}$$

and by neglecting the acoustic mass

$$R_s = \varrho_0 c; \qquad \text{if} \qquad kr \gg 5, \tag{6.7}$$

r denoting the radius of the tube. The impedance analysis of an organ pipe can be done by numerical means, using the boundary element method. The comparison of the results of analytic computation and simulation by the BEM can be seen in figure 6.4.

Despite, that in case of the piston problem, the piston is considered to be perfectly rigid, which would be a very rough approximation of the resonating air column, the similarity of the two curves is remarkable. It is also worth to mention, that for high frequencies the curves converge to the value of $\varrho_0 c$, which approximately equals to 420 Rayl, using the given constants of the sound speed and average density. (Note, that the analytic resistance-mass analogy is not valid for high frequencies ($kr \gg 5$), and a simple resistance with a value of $\varrho_0 c$ can be used instead.)

The analysis of the terminating impedances gives an explanation of some attributes of the pipe transfer function.

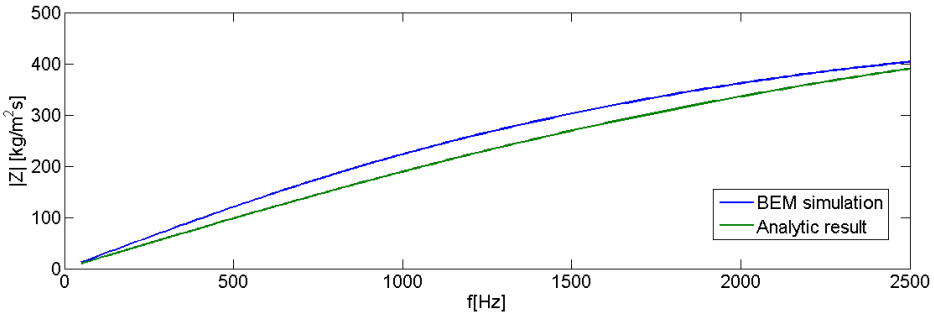

Figure 6.4: Comparison of analytic and simulation results of the terminating impedance of a cylindric pipe with one end open. $L = 857.5$ mm; $r = 42$ mm.

- The end correction formula and thus, the shifting of the fundamental frequency can be understood taking into consideration that the finite values of the terminating impedance is not equivalent to the ideal $p = 0$ case, which prescribes zero impedance for the open end.
- The stretching effect is caused by the frequency dependence of the terminating impedances. Since the value of the terminating impedances are higher for higher frequencies, the frequencies of the longitudinal modes become more and more stretched.
- Decreasing Q-factors of eigenresonances are partly caused by the increasing values terminating impedances. The other effect that determines the Q-factor of a certain resonance is the damping factor of air, which is also frequency dependent.

Analytic solutions can not take into account that the radiation impedance is not only dependent of the frequency, but also varying spatially over the openings of the pipe. The distribution of the impedance values in case of a cylindric pipe can be seen in figure 6.5, while the same for a rectangular pipe is shown in figure 6.6.

The impedance values near the edges are approximately half of the values near the center of the cross section. This means that the analytic approximation, which regards these impedances independent of the location, can not be successfully applied as boundary conditions in simulations. As seen, the distribution of the terminating impedance values is not, or just negligibly dependent of the frequency.

Making use of the facts, that the values of terminating impedances are varying slowly with respect to the frequency, and that their distribution over the cross section is nearly independent of the frequency, interpolation formulae can efficiently be applied in the coupled FE/BE method.

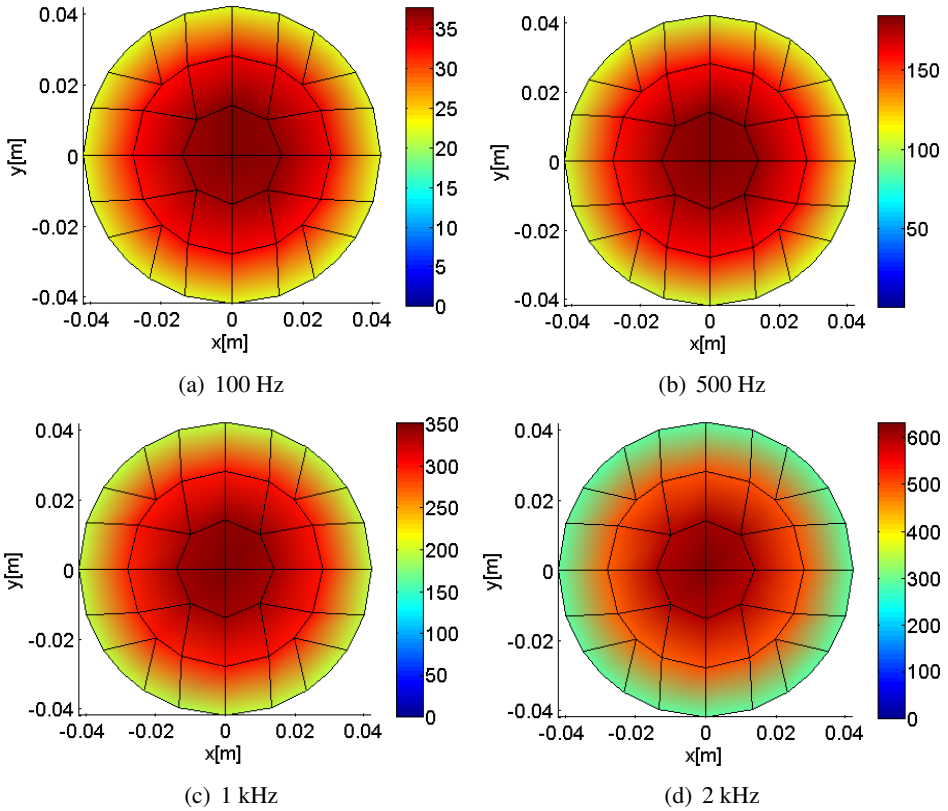

(a) 100 Hz

(b) 500 Hz

(c) 1 kHz

(d) 2 kHz

Figure 6.5: Distribution of terminating impedance at the open end in case of a cylindric pipe

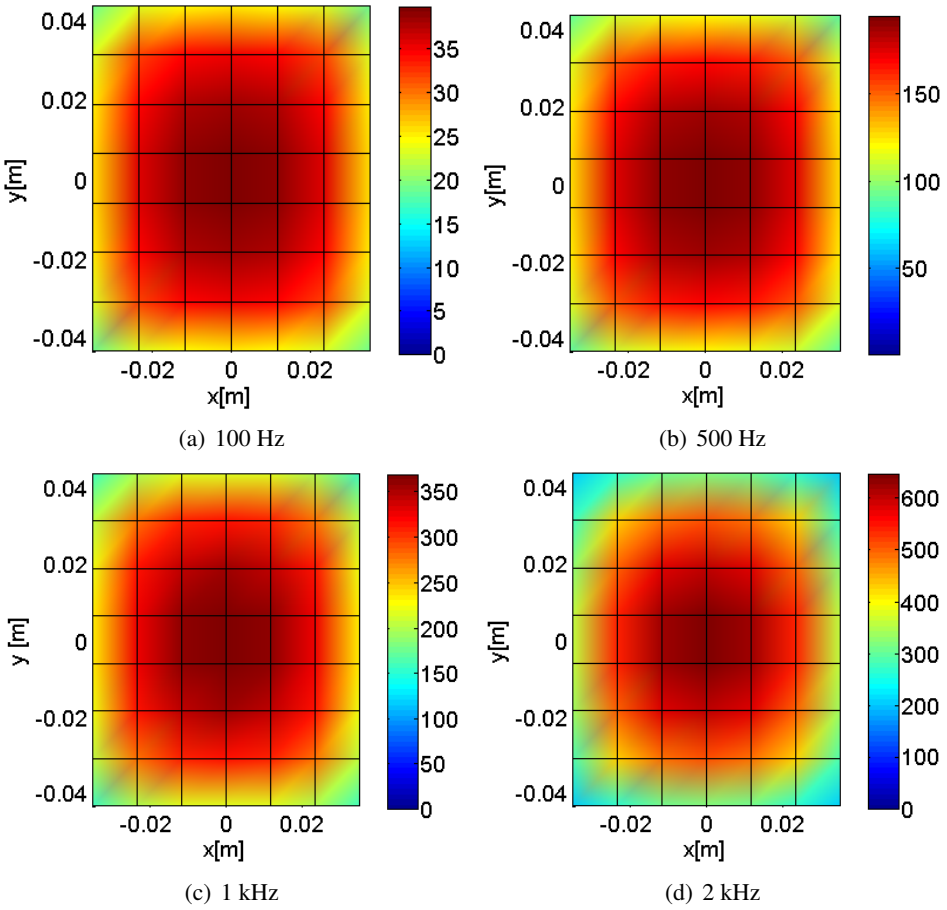

(a) 100 Hz

(b) 500 Hz

(c) 1 kHz

(d) 2 kHz

Figure 6.6: The distribution of terminating impedance at the open end in case of a rectangular pipe

6.4 Pipe simulations

Pipe simulations were run on a series of wooden flue organ pipes, which already have been built and measured at the Fraunhofer Institut für Bauphysik, Stuttgart. These pipes were designed as a part of an experiment that examined how the dimensioning affects the sounding of wooden pipes. Therefore these pipes had different geometrical parameters, but similar steady sound characteristics, and were appropriate subjects for test simulations. The experiment is described in [14] in detail. The series consisted of five pipes of C tone, three from these were chosen and made simulation models of. Table 6.3 shows the exact dimensions of these pipes (4/16, 4/18 and 4/20 mean mouth width to circumference ratio).

Pipe	Length	Width	Depth	Mouth height	Mouth width
4/16	1180	69.80	86.87	19.87	68.64
4/18	1181	61.20	98.32	21.53	60.76
4/20	1179	55.34	108.40	25.34	53.93

Table 6.3: Pipe dimensions given in mm

The meshes were generated using a self developed, parametric mesh generator script. According to measurement data, cut-off frequencies of these pipes were in between 1.5 and 2 kHz. Hence, maximal element size was chosen not to be greater than 17.5 mm, which resulted a maximal validity frequency of approximately 2.5 kHz, making use of equation (5.1). At the mouth part, the model resolution was set higher to be able to follow the steep changes of acoustical variables near the free edges of the geometry.

Simulations were run by using both the indirect BEM and the coupled FE/BE method. Testing frequencies were chosen to start from 50 Hz and end at 2500 Hz with a 1 Hz resolution. In case of the coupled method, the Schur complement and interpolation technique were applied. The interpolation was carried out using a spline formula with 30 base points. The surface meshes consisted of approximately 1500 nodes, while the volume mesh had 2500 nodes.

Computational times were around 6 and $6\frac{1}{2}$ hours using the indirect BEM, and between 6 and 8 hours using the coupled method on the same computer. It is worth mentioning, that the coupled method under a self developed program performed nearly as fast as the indirect method under the commercial software package. This means that a more optimized implementation of the coupled method would perform very well in simulations.

In the following tables and figures simulation results are compared to each other and measurement data. Frequencies of the first five harmonics and stretching

factors were examined. Q-factors of these modes were also given among measurement data, but to be able to determine real Q-factors a damping model of air should be applied, which was not implemented herein. Thus, Q-factors determined by simulations can only be examined qualitatively, as without a damping model, simulated Q-factors are much higher than the real ones.

Tables 6.4, 6.5 and 6.6 show comparison of acoustical parameters of the pipes, while figures 6.7, 6.8 and 6.9 show diagrams of simulated spectra at the pipe mouth.

Pipe: 4/16	**Measurement**		**Indirect BEM**		**Coupled FE/BE**	
Harmonic	F [Hz]	Stretch	F [Hz]	Stretch	F [Hz]	Stretch
1. (Fund.)	129.87	1.000	131	1.000	128	1.000
2. (Octave)	261.76	2.016	263	2.008	253	1.977
3.	396.45	3.053	397	3.031	388	3.031
4.	536.98	4.135	531	4.053	522	4.078
5.	677.62	5.218	667	5.092	660	5.156
Cut-off [Hz]	1987		1987		2008	

Table 6.4: Comparison of measurement and simulation results for the 4/16 pipe

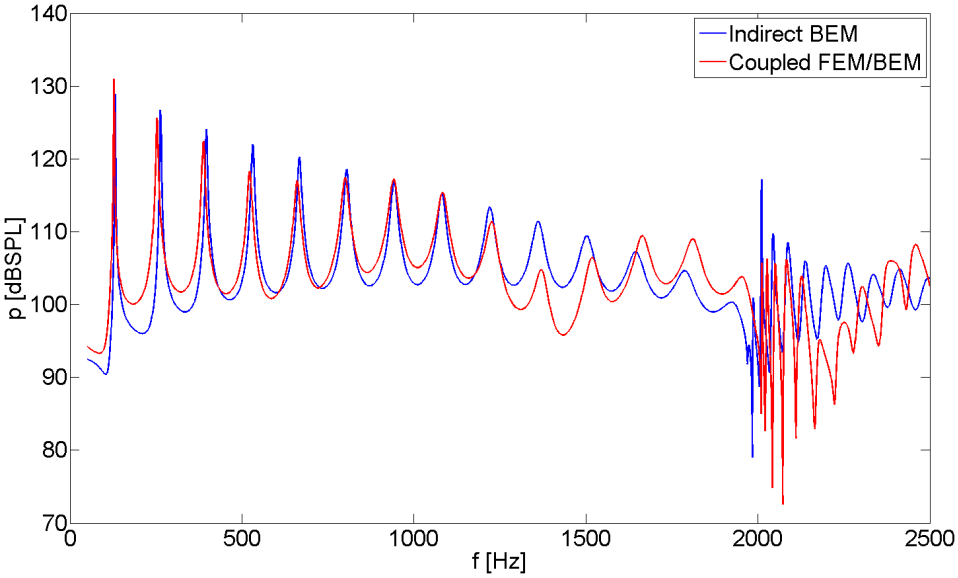

Figure 6.7: Comparison diagram of simulation results for the 4/16 pipe

The fundamental frequencies are approximated within 1% range by the indirect boundary method, this means an absolute deviation that is less than 1.5 Hz. The

Pipe: 4/18	**Measurement**		**Indirect BEM**		**Coupled FE/BE**	
Harmonic	F [Hz]	Stretch	F [Hz]	Stretch	F [Hz]	Stretch
1. (Fund.)	131.22	1.000	130	1.000	128	1.000
2. (Octave)	262.44	2.000	262	2.008	252	1.969
3.	400.38	3.051	394	3.025	387	3.023
4.	547.08	4.169	529	4.056	521	4.070
5.	680.99	5.190	664	5.095	660	5.156
Cut-off [Hz]	1740		1741		1768	

Table 6.5: Comparison of measurement and simulation results for the 4/18 pipe

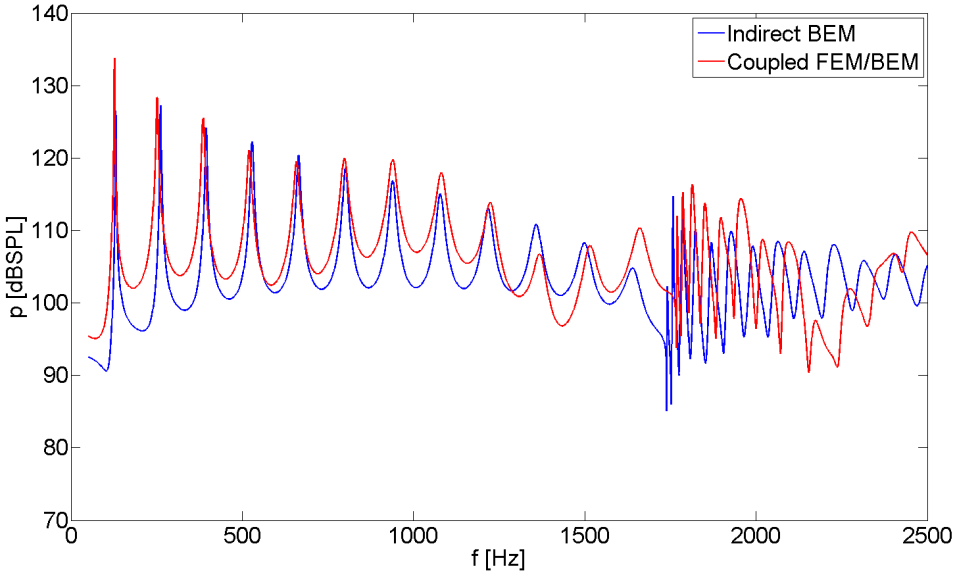

Figure 6.8: Comparison diagram of simulation results for the 4/18 pipe

coupled method predicts the fundamental frequencies with the average error 2-3% below the measured value. The maximal deviation is experienced in case of the 4/20 pipe, where the error is 5 Hz. This error is acceptable considering the simplicity of the model. The 1% deviance in case of the indirect BEM method is satisfactory and would alse be acceptable for an industrial application.

In case of the 4/16 and the 4/18 pipe the coupled method showed some irregularities for the octave and determined the stretching factor with significant error. The deviation of the measured and simulated frequencies is around 4-5% for these two pipes. For the further harmonics the coupled method estimates the stretching factors more accurately than the indirect method. However, the frequencies

Pipe: 4/20	**Measurement**		**Indirect BEM**		**Coupled FE/BE**	
Harmonic	F [Hz]	Stretch	F [Hz]	Stretch	F [Hz]	Stretch
1. (Fund.)	131.22	1.000	130	1.000	126	1.000
2. (Octave)	265.12	2.020	262	2.007	255	2.024
3.	401.73	3.061	395	3.024	388	3.079
4.	543.71	4.143	529	4.053	524	4.159
5.	679.64	5.190	665	5.095	662	5.254
Cut-off [Hz]	1582		1579		1599	

Table 6.6: Comparison of measurement and simulation results for the 4/20 pipe

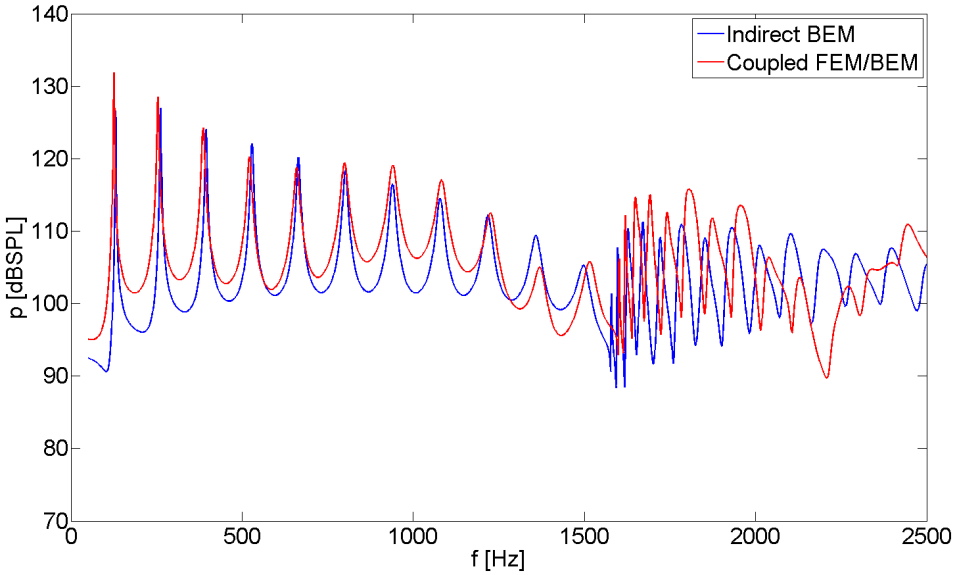

Figure 6.9: Comparison diagram of simulation results for the 4/20 pipe

of these partials are generally determined more accurately by the indirect method, with a maximal error of 4%.

The cut-off frequencies are determined accurately by the indirect BEM and within a 1.5% error range by the coupled technique. This is a very accurate result taking into consideration that the resonater model implies remarkable simplification and neglects. The resulting cut-off frequencies are lower for the deeper pipes, as it is expected. Above the cut-off frequencies, the spectra become irregular as expected. As the irregularities are very sensitive to the model parameters, the simulated spectra are not expected to match up above the cut-off. In this frequency range the spectrum is not examined in details, only the cut-off effect is important.

Parameter	Indirect BEM	Coupled FEM/BEM
Fundamental frequency	<1%	2-4%
Octave frequency	<1%	3-5%
Further partials	2-4%	2-5%
Stretching factors	2-3%	<2%
Cut-off frequency	<1%	<1.5%

Table 6.7: Comparison of relative errors of the two numerical methods

Comparing the diagrams to figure 2.3, it can be seen, that the simulated transfer functions qualitatively correspond to a typical pipe transfer function. The amplification peaks are wider for the successive harmonics, as expected. The detailed analysis of Q-factors is not done herein, because of the reasons mentioned above.

As it can be seen on the comparison diagrams, minor irregularities are experienced in simulation results involving the coupled FE/BE method around 1.5 kHz. It is possible that it is caused by the meshing problem described in chapter 5. The examination of these irregularities and some other minor issues concerning the coupled method are not examined here in more detail.

Except for the mentioned irregularities, as it can be seen, the simulated spectra approximately match up for the two methods. Therefore, both methods can efficiently be applied for pipe simulations. The accuracy analysis of the two methods is summarized in table 6.7.

A chimney pipe experiment

Beside the simulations of wooden pipes a chimney pipe experiment was performed by using the indirect BEM. The chimney pipe is named after the small 'chimney' tube that is attached to the resonator body. The geometry is shown in figure 5.2, on the right side. As seen, the resonator geometry is more complicated than in case of wooden pipes. Table 6.8 shows the exact dimensions of the pipe.

Parameter	Value
Resonator length	586.0
Resonator diameter	81.1
Chimney length	162.2
Chimney diameter	20.3
Mouth height	22.0
Mouth width	59.9

Table 6.8: Dimensions of the chimney pipe given in mm

Only the fundamental frequency was given beside the geometry parameters.

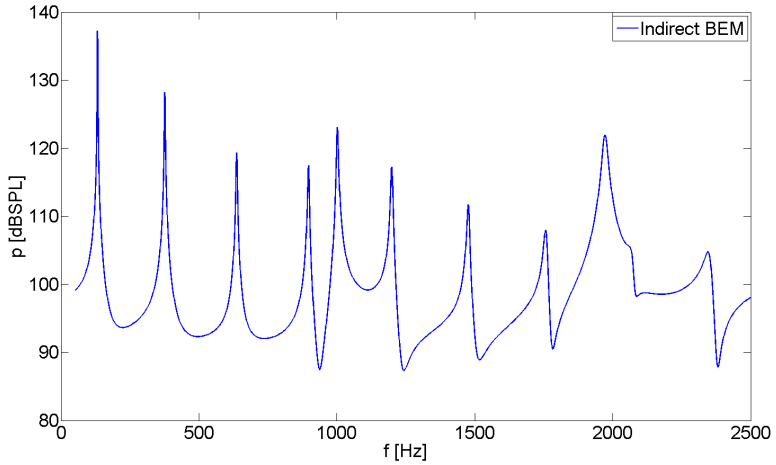

Figure 6.10: Simulated transfer function of a chimney pipe

This had the value of 130.8 Hz according to measurement results. The indirect BEM simulation gave 131 Hz for the fundamental frequency, which is accurate, as the simulation was run with the resolution of 1 Hz. The simulated spectrum at the pipe mouth can be seen in figure 6.10.

As this experiment was not in the main line of the research, the results are presented as an example of application of the indirect BEM for a special mesh. It is worth mentioning that the same C tone is achieved by a completely different pipe geometry and dimensioning. This experiment was demonstrated here only as an outlook on further simulations that can be carried out by using the presented numerical techniques.

6.5 PML experiments

Since there is no commercial software available that contains the implementation of acoustical perfectly matched layers, the author developed a simulation program under `Matlab` environment, which implements the PML for a one dimensional case, as described in chapter 4. The simulation setups for PML tests is shown in figure 6.11.

The first test was a comparison between the two models shown in figure 6.11. The first model is a simple classical finite element model with no absorbing layers attached. In the second case a PML layer of several elements is attached to both ends of the FE model. The excitation is given as a prescribed normal velocity at the middle node of the model, i.e. the $x = 0$ location. The classical FE model is

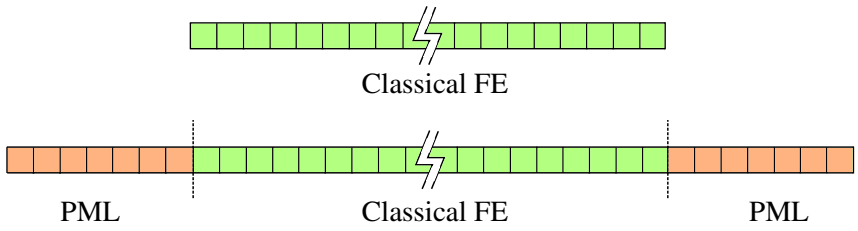

Figure 6.11: Simulation setups for PML experiments

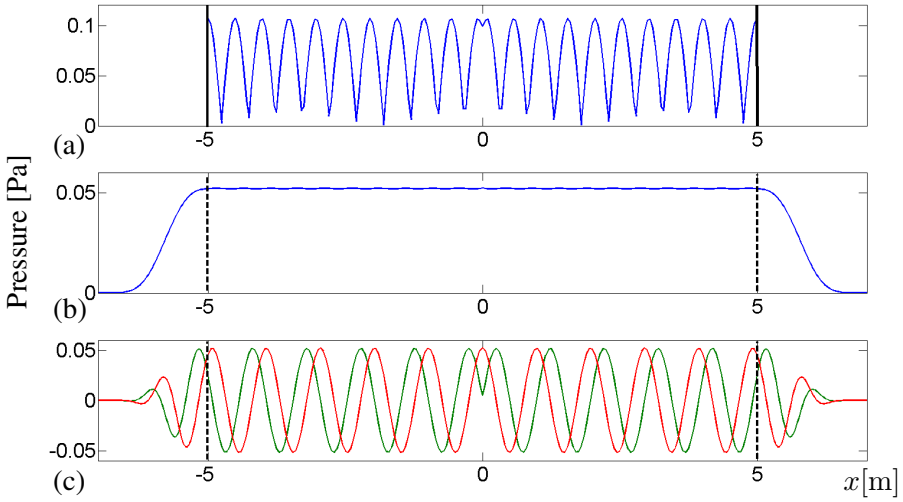

Figure 6.12: Operation of the 1-D PML model. Explanation in the text.

expected to have pressure waves reflected back from the enclosures, and therefore standing waves evolving dependent of the testing frequency. At the same time, the absorbing layer is designed to have zero reflections on the boundary, and thus, propagating waves are expected. The comparison is shown in figure 6.12.

Diagram 6.12.a. shows the absolute value of pressure for the classical FEM case. Heavy reflections from the boundaries are experienced and standing waves evolve in the medium. The operation of the absorbing layer is shown in diagrams 6.12.b-c., where the pressure amplitude (blue) and real (red) and imaginary (green) parts are displayed. One can see, that the amplitude of the pressure wave vanishes in the perfectly matched layers. The imaginary and real parts are in $\frac{\pi}{2}$ phase in the whole domain, which is the property of a propagating wave. This experiment shows that the PML can perform well as an absorbing layer.

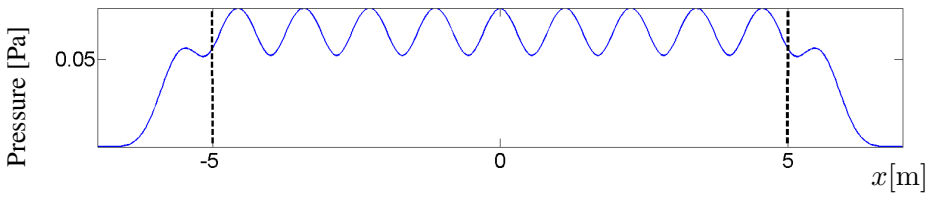

Figure 6.13: Example of instable behavior of the PML

Unfortunately, the good performance is not automatic, as the behavior of the perfectly matched layer is very sensitive to the damping parameters. The former experiment had shown the performance of the layer at 350 Hz. The behavior of the same layer at 150 Hz is shown in figure 6.13.

As it is seen, in the latter case the PML did not act as it was expected to. Despite of the fact, that the amplitude vanishes in the layer, significant reflections are experienced. This can be caused by a damping function that is too steep. In the following, PML behavior will be examined with respect to changing the parameters, i.e. layer thickness, discretization roughness and the parameters of the damping function. A parabolic damping function will be used for the following experiments, which defines the damping parameter as $\sigma_1 = kx^2$, where k is the damping constant and x denotes the depth inside the layer. Using a paraboloid function ensures fast decaying and continuity at the artificial boundary.

The performance of the PML can be measured by the amplitude of the pressure wave that is reflected back into the region of interest. These reflected waves cause appearance of standing waves in the interior domain. Therefore, in the following experiments the error is represented by the ratio of the amplitude of the reflected wave and outgoing wave. This can be approximated using the ratio of the maximal and average amplitude.

Figure 6.14 shows comparison performance of perfectly matched layers with different discretization fineness and different damping function steepness. In the diagram on the left hand side the length of PML elements, l was the parameter, while the $k = 500\pi$ and $w = 2$ m damping constants and layer widths were used. For the curves in the right hand side diagram, k was variable and $l = 25$ mm and $w = 2$ m constants were set.

As it can be seen, increased resolution results in better performance in the high frequency domain, while it has no effect for lower frequencies. This means that there is a minimum number of PML elements in a wavelength, like in the FEM, where this number should be eight at least. On the right hand side diagram it is shown, that a steep damping functions performs poorly in the low frequency range, while it causes small errors in case of higher frequencies. A flatter damping

function results in smaller errors for low frequencies, but it also implies instabilities at high frequencies.

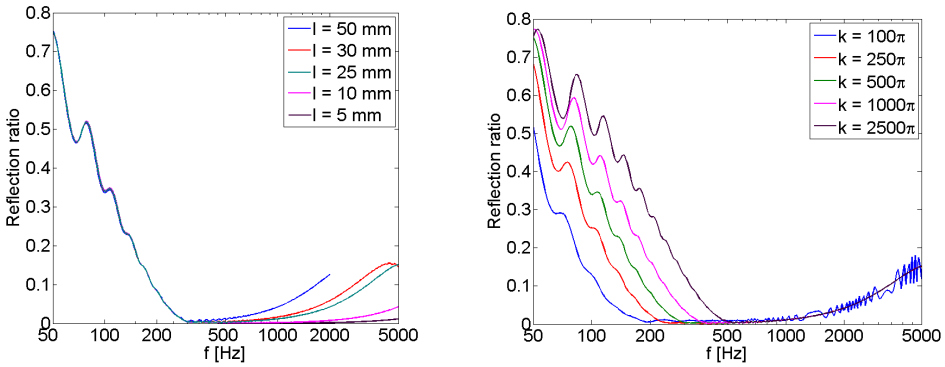

(a) Different resolutions (b) Different damping functions

Figure 6.14: Performance of PMLs with different resolutions and damping functions

Comparison of PMLs with different layer width and damping parameters are shown in figure 6.15. In these experiments the length of the PML element was set to be constant. $l = 2.5$ cm was set for lower frequencies (left hand side diagram), while $l = 1$ cm was used for the higher frequency range (right hand side diagram).

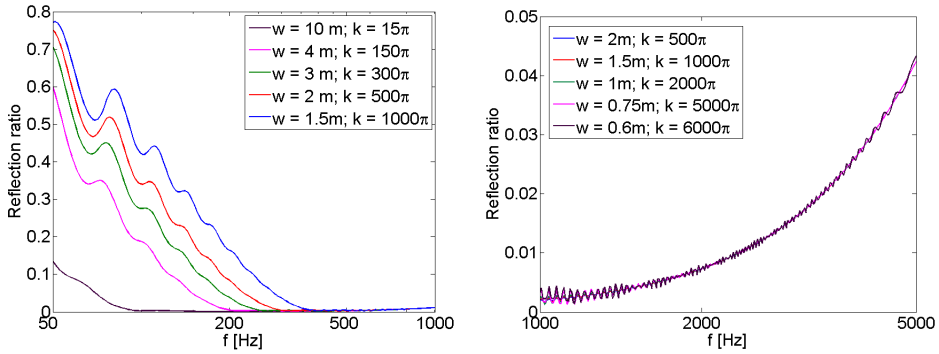

(a) Low frequency (b) High frequency

Figure 6.15: Performance of PMLs with different layer widths

Since the same damping performance can be achieved by a wider layer with a flat damping function and by a narrower layer with a steep damping function, the damping parameter k was also changed with respect to the different w values. As it can be seen in the diagrams, a wider layer performs well for low frequencies two, while for higher frequencies narrower layers can be used paired with steep damping

functions. Too wide layers are inefficient for higher frequencies, as the element size has to be smaller for smaller wavelengths, and a wide layer would require a high number of damping elements, which implies enormous raise of computational effort. On the other hand narrow layers can be used for high frequency simulations. This way, the number of PML elements can be constant for the certain frequency ranges.

As seen, a compromise must be made in the application of the PML, as good performance for the entire frequency range requires a very large number of PML elements. Even so, by setting up the appropriate damping parameters, the PML can perform very well as an absorbing boundary. That is why current researches investigate the optimization of perfectly matched layers, see [7, 9, 15].

Naturally, the one dimensional perfectly matched layer can not be used in real applications, but the two and three dimensional implementations can be derived from this simplest case. A three dimensional PML will be able to be used for organ pipe simulation, surrounding the vicinity of the pipe resonator with damping elements. Further examination, optimization and a 3D implementation of the PML method are included in the author's future plans.

Chapter 7

Epilogue

7.1 Conclusions

It was shown, that the indirect boundary element method and the coupled FE/BE method can be applied for the calculation of the steady sound field of an organ pipe resonator. These methods are unable to model the sound generation process in its whole complexity. Despite of the fact, that the acoustic model contains significant neglects and simplifications, some key parameters on the sounding can be determined using these methods.

Frequencies of the fundamental and other harmonics, stretching factors and cut-off frequencies were compared to each other and measurement data. Generally, the indirect BEM method gave a more accurate result for the frequencies of the partials, while stretching factors were approximated more accurately by the coupled method. The cut-off frequencies were predicted with sufficient accuracy by both methods.

It was also shown, that for a more detailed examination of the sounding characteristics, e.g. the analysis of Q-factors the acoustical model should be extended. This is also included in my future plans.

The PML method was tested for a simple case, and as it was seen, it is able to act like an absorbing boundary, if the parameters of the layer are set properly. Therefore, it would be possible to apply PMLs for pipe simulations by an appropriate implementation.

All in all, it can be stated, that numerical techniques in acoustics can successfully be applied for the simulation of organ pipes. For an industrial application of simulation methods, models with higher resolution should be used, ensuring the required accuracy.

7.2 Future work

My future plans are the following. The PML method should be implemented for a three dimensional case, to be able to set up pipe simulations using this method. Further examination of PML implementations and damping parameters should be carried out to maximize the efficiency of the absorbing layer. It would also be useful to implement other numerical techniques such as infinite elements or other types of artificial boundaries. In order to be able to increase the resolution of the model, optimization and further speed up techniques should be applied. The coupled method should also be further optimized and tested for different pipe geometries with various resolutions.

To enhance the accuracy of the simulations, the pure acoustical model should be extended with physical parts, by which resonances of the mechanical structure of the pipe could be examined by means of a coupled vibroacoustic model. My long term plan is to examine the sound generation mechanism by taking into consideration the fluid flow effects. To be able to do this the analysis of a non-linear coupled model needs to be done. By the simulation of these effects attack transients could be calculated, for example.

Summary

It was shown in my master's thesis how can organ pipes be modeled by means of numerical acoustics. Simulation experiments were set up and performed using commercial and self developed software. The results were compared to measurement data, that were already available. The main steps of the course of the work are summarized in the following.

Firstly, the structure and functional principles of pipe organs and the attributes of the sound generation process were examined. Simplifications, which are necessary in order to be able to model the problem by means of numerical techniques were presented. Acoustical parameters that can be determined from the pipe transfer function were reviewed.

The fundamentals of linear acoustic were summarized and a deduction of the acoustic wave equation was given. Some of the intermediate results were used in the application of numerical methods. The weak form of the boundary value problem was deduced, which is the first basis of the discretization process of the finite element method.

The acoustical finite and boundary element methods were discussed in detail. Making use of these two a coupled FE/BE technique was deduced, which was implemented by self developed software. The techniques by which computation can be sped up for the coupled model were also examined and explained. These options were also applied in pipe simulations. By the Schur's complement and the interpolation techniques the coupled method can be sped up significantly, without causing considerable error.

Meshes of various organ pipes with different dimensions were set up, using a parametric algorithm. Simulations were performed using the indirect BEM and the coupled FE/BE method. The simulation results were compared with measurement data. It can be assessed that some key parameters of the sounding can be determined with sufficient accuracy by means of numerical techniques, taking into consideration the simplifications and neglects of the model. The possibilities of extending the model were summarized, in order to get a better insight into the sound generation and to be able to simulate further phenomena, such as transient response of the pipes.

The PML technique was examined as an alternative way of modeling the free sound field. A deduction of the anisotropic wave equation for the PML was given and the PML was implemented for a one-dimensional case using a finite element discretization. The performance of perfectly matched layers with different damping parameters were analyzed. My experiments showed, that a three dimensional, improved implementation of the PML can be suited to set up an environment for organ pipe simulation.

Összefoglalás

Diplomamunkámban megmutattam, hogy hogyan modellezhetőek az orgonasípok a numerikus akusztika eszközeivel. Szimulációs elrendezéseket állítottam össze, majd a szimulációkat kereskedelmi és saját fejlesztésű szoftverekkel futtattam. Az eredményeket már meglévő mérési adatokkal vetettem össze. Munkám fontosabb lépéseit foglaltam össze az alábbiakban.

Megismerkedtem az orgonák szerkezetével, illetve a hangkeltési mechanizmus jellegzetességeivel. Megmutattam azokat a szükséges egyszerűsítéseket, amelyek lehetővé teszik, hogy a probléma vizsgálható legyen a numerikus akusztika eszközeivel. Ismertettem azokat az akusztikai paramétereket, amelyek meghatározhatóak a síp átviteli függvényének ismeretében.

Összefoglaltam a lineáris akusztika alapösszefüggéseit, bemutattam a hullámegyenlet levezetését, melynek részeredményeit később felhasználtam numerikus technikák alkalmazásakor. Levezettem a peremérték probléma gyenge alakját, ami a kezdeti lépése a végeselem módszernél alkalmazott diszkretizálási technikának.

Elsajátítottam az akusztikai végeselem és peremelem módszereket. Ezeket felhasználva levezettem egy csatolt módszert, melynek megoldását saját programmal implementáltam. Megvizsgáltam a csatolt módszernél alkalmazható gyorsítási lehetőségeket, melyeket alkalmaztam is a sípok szimulációja során. Elmondható, hogy a Schur komplemens technikával és az admittancia feltételek számítására alkalmazható interpolációs eljárás segítségével a csatolt módszer jelentősen felgyorsítható, anélkül, hogy ezzel számottevő hibát okoznánk.

Paraméterezhető algoritmus segítségével geometriai modelleket hoztam létre többféle síphoz. Szimulációkat futtattam az indirekt peremelem és a csatolt módszer segítségével. A szimulációs eredményeket valós mérési eredményekkel hasonlítottam össze. Elmondható, hogy a modellalkotáskor alkalmazott elhanyagolásokat figyelembe véve a hangzás egyes paraméterei megfelelő pontossággal számíthatóak numerikus eljárások alkalmazásával. Összefoglaltam azokat a kiegészítő lehetőségeket, amelyekkel a modellt továbbfejlesztve pontosabb képet kaphatunk a hangzásról, illetve további, például tranziens jelenségek szimulációjára is lehetőség nyílik.

A szabad hangtér egy alternatív modellezési lehetőségeként vizsgáltam a PML módszert. A felhasznált irodalmak alapján levezetést adtam a PML anizotróp hullámegyenletére. Bemutattam a PML egy végeselem megvalósítását, melyet implementáltam az egydimenziós esetre. Összehasonlítottam különböző paraméterekkel rendelkező rétegek csillapítási tulajdonságait. Kísérleteim alapján megállapítható, hogy a PML háromdimenziós továbbfejlesztése alkalmas lehet orgonasíp szimulációs környezet kialakítására.

Acknowledgments

I would like to thank Assoc. Prof. Fülöp Augusztinovicz, prime supervisor of my thesis, for leading my research, giving me encouragement for this project and making the equipment of the laboratory available for me. I shall thank him for accepting me as a member of his team too.

I specially thank Dr. Péter Fiala for the regular consultations and for reviewing my thesis several times. I must also thank him for letting me to use the `AcouBEM` and `AcouFEM` software and for his valuable hints concerning `Matlab` programming and usage of LaTeX.

I express my gratitude as well to Dr. Judit Angster, head of Group of Musical acoustics of the Fraunhofer Istitut für Bauphysik in Stuttgart, for her valuable remarks and the measurement and pipe geometry data that she has made available for me.

Most of this research was supported by the European Commission (Research for SMEs, Contract No: 222104) and by 10 European organ builder firms.

Last but not least, I shall thank my family for always giving me encouragement, understanding and care during my university years.

Bibliography

[1] J. Angster. State of the art measurement techniques and results of sound generation and vibration of labial organ pipes, 1990. Candidate's thesis. In Hungarian.

[2] X. Antoine, M. Darbas, and Y. Y. Lu. An improved surface radiation condition for high-frequency acoustic scattering problems. *Computational Methods in Applied Mechanical Engineering*, 195:4060–4074, 2006.

[3] R. J. Astley. Infinite elements. In Marburg and Nolte [22], pages 199–230.

[4] U. Basu and A. K. Chopra. Perfectly matched layers for time-harmonic elastodynamics of unbounded domain: theory and finite-element implementation. *Computational Methods in Applied Mechanical Engineering*, 192:1337–1375, 2003.

[5] L. L. Beranek. *Acoustics*. Acoustical Society of America, 1986.

[6] J.-P. Bérenger. A perfectly matched layer for the absorption of electromagnetic waves. *Journal of Computational Physics*, 114:185–200, 1994.

[7] A. Bermúdez, L. Hervella-Nieto, A. Prieto, and R. Rodrígez. Perfectly matched layers. In Marburg and Nolte [22], pages 167–196.

[8] J. Biermann, O. von Estorff, S. Petersen, and C. Wenterodt. Higher order finite and infinite for the solution of Helmholtz problems. *Computational Methods in Applied Mechanical Engineering*, 2009. Article in press.

[9] F. Collino and P. B. Monk. Optimizing the perfectly matched layer. *Computational Methods in Applied Mechanical Engineering*, 164:157–171, 1998.

[10] J. P. Coyette and J. Van de Peer. Acoustic Boundary Elements. In Sas [28], chapter VII.

[11] J. Diaz and P. Joly. A time domain analysis of PML models in acoustics. *Computational Methods in Applied Mechanical Engineering*, 195:3820–3853, 2006.

[12] D. Dreyer, S. Petersen, and O. von Estorff. Effectiveness and robustness of improved finite elements for exterior acoustics. *Computational Methods in Applied Mechanical Engineering*, 195:3591–3607, 2006.

[13] P. Fiala. AcouFEM developer and user's guide, 2008. Unpublished.

[14] Elena Esteve Fontestad. Innovative method for the development of optimal scaling of the depth and width of wooden organ pipes. Master's thesis, Universidad Politécnica de Valencia, 2008.

[15] D. Givoli. Computational absorbing boundaries. In Marburg and Nolte [22], pages 145–166.

[16] D. Givoli, T. Hagstrom, and I. Patlashenko. Finite element formulation with high-order absorbing boundary conditions for time-dependent waves. *Computational Methods in Applied Mechanical Engineering*, 195:3666–3690, 2006.

[17] P. Göransson. Acoustic Finite Elements. In Sas [28], chapter VI.

[18] J. Granát. Physics of musical instruments, 2009. In Hungarian.
URL : http://vibac.hit.bme.hu/documents/117hangszerekfizikaja.zip.
Last accessed in May, 2009.

[19] I. Harari. A survey of finite element methods for time-harmonic acoustics. *Computational Methods in Applied Mechanical Engineering*, 195:1594–1607, 2006.

[20] I. Harari and U. Albocher. Studies of FE/PML for exterior problems of time harmonic elastic waves. *Computational Methods in Applied Mechanical Engineering*, 195:3854–3879, 2006.

[21] C. Ianculescu and L. L. Thompson. Parallel iterative solution for the Helmholtz equation with exact non-reflecting boundary conditions. *Computational Methods in Applied Mechanical Engineering*, 195:3709–3741, 2006.

[22] S. Marburg and B. Nolte, editors. *Computational Acoustics of Noise Propagation in Fluids – Finite and Boundary element methods*. Springer, 2008.

[23] S. Marburg and B. Nolte. A unified approach to finite and boundary element discretization in linear time-harmonic acoustics. In *Computational Acoustics of Noise Propagation in Fluids – Finite and Boundary element methods* [22], pages 1–34.

[24] A. Miklós and J. Angster. Sound radiation of open labial organ pipes; the effect of the size of the openings on the formant, 1998. Abstract from ISMA '98 conference documentation. Leavenworth, Washington, USA.

[25] A. Miklós and J. Angster. Properties of the sound of flue organ pipes. *Acta Acoustica*, 86:613–615, 2000.

[26] Q. Qi and T. Geers. Evaluation of the perfectly matched layer for computational acoustics. *Journal of Computational Physics*, 139:166–183, 1998.

[27] S. K. Richards, X. Zhang, X. X. Chen, and P. A. Nelson. The evaluation of non-reflecting boundary conditions for duct acoustic computation. *Journal of Sound and Vibration*, 270:539–557, 2004.

[28] P. Sas, editor. *Advanced Techinques in Applied and Numerical Acoustics*. Katholieke Universitiet Leuven, 1997.

[29] G. Szoliva. Effects of voicing methods on the sound generation process in case of open labial organ pipes. Master's thesis, Budapest University of Technology and Economics, 2005. In Hungarian.

[30] L. Zhao and A. C. Cangellaris. A general approach for developing unsplit-filed time-domain implementations of perfectly matched layers for FDTD grid truncation. *IEEE Transactions on Microwave Theory and Technology*, pages 2555–2563, 1996.